UNIVERSIDAD AUTÓNOMA DE SAN LUIS POTOSÍ

FACULTAD DE CIENCIAS

Anisotropies, electronic and magneto-optic properties in low and alloy concentrations of Gd-doped CeO_2 thin films using a strain-optical approach.

TESIS

PARA OBTENER EL GRADO DE:

DOCTOR EN CIENCIAS APLICADAS

PRESENTA:

José Gabriel Roberto Hernández Arteaga

DIRECTOR DE TESIS:

Ángel Gabriel Rodríguez Vázquez

SAN LUIS POTOSÍ, SLP JUNIO 2022

TESIS DE DOCTORADO.

Anisotropies, electronic and magneto-optic properties in low and alloy concentrations of Gd-doped CeO_2 thin films using a strain-optical approach.

José Gabriel Roberto Hernández Arteaga.

COMITÉ QUE ACEPTA LA TESIS

Dr._____ Asesor _____

Dr._____ Sinodal _____

Dr._____ Sinodal _____

Dr._____ Sinodal _____

Dr._____ Sinodal _____

UNIVERSIDAD AUTÓNOMA DE SAN LUIS POTOSÍ

Anisotropies, electronic and magneto-optic properties in low and alloy concentrations of Gd-doped CeO_2 thin films using a strain-optical approach.

José Gabriel Roberto Hernández Arteaga.

*In partial Fulfillment of the Requirements for the degree of Doctor of Philosophy in **Applied Science**.*

Supervisor:

Ángel Gabriel Rodríguez Vázquez.

CIACYT-CARIEM department June 2022.

CONTENT.

“De nuestros miedos nacen nuestros corajes

Y en nuestras dudas viven nuestras certezas

Los sueños anuncian otra realidad posible

Y los delirios otra razón

En los extravíos no esperan los hallazgos

Porque es preciso perderse para volver a encontrarse”

Un enigmático profesor.

Como cada mañana aquel día me levanté, tomé de la mesa mi portafolio al que observé por unos segundos preguntándome si dentro se encontraban las copias del material que con días de antelación había procurado imprimir para las clases del día, acto seguido me inundó el pensamiento de que mi portafolio comenzaba a notarse gastado sintiendo la necesidad de cambiarlo, a lo que automáticamente compensé de manera amigable, "*bueno, seguramente es un lujo que no nos podemos dar aquellos que pertenecemos al gremio de pobresor hora-clase*", al cerrar la puerta y recorrer las primeras calles rumbo a la facultad de derecho, mi cerebro, como si de una función sobreyectiva se tratase comenzó a no dejar elementos por relacionar con las cosas que había pasado por alto antes de abandonar el recinto, como peinarme, el desayuno o la loción, pero que fueron interrumpidos por la sutil emoción de que aquel mismo día comenzaba el curso de *algebra superior* para los alumnos de nuevo ingreso en la facultad de ciencias, "¿Estaría bien comenzar con la historia del niño Gauss, un precoz de las matemáticas?, ¿Les hablaré del capítulo de las matemáticas sobre el duelo de cúbicas?, ¿De la conjetura de Fermat?, sin notarlo me encontraba ya en el aula de clases. Al terminar los alumnos se dispusieron a abandonar el salón en pequeños grupos que sin notarlo formaban números primos, ¿Ellos lo sabrían? ¿Lo habrán hecho a propósito?, quise por un momento comentarlo con el último de ellos, pero la prisa con esa juventud le gana a cualquier simple observación. Me dirigí por avenida Cuauhtémoc hacia la Facultad de Ciencias, de reojo pude ver a aquel montículo amarillo pasar a mi lado y comenzó a surgir la creciente sensación de tomarlo, de inmediato recordé que a estas alturas de la vida era la única actividad que me mantenía en forma y se acercaba ya el medio maratón universitario, ¡ah! ¿Cuánto tiempo había pasado desde que había tomado la decisión de no entrenar más?, me transporté de pronto a aquel olor a arcilla húmeda y por unos momentos la sensación de haber cerrado una serie de 400m en 1:05 después de la sexta repetición me recorrió el cuerpo, tanto que mis lentos pasos comenzaron a acelerarse y fueron tomando la forma de un ligero trote, provocando una euforia tal que la sensación me recordó al momento en que mis ojos habían contemplado como Bekele había conquistado aquél doblete y seguro de lo que mis ojos acababan de presenciar me convencí de que tendría que pasar muchísimo tiempo para que otro ser humano lo volviera a conseguir, no obstante unas semanas más tarde me retractaría de tan fatal afirmación, con un amargo sabor de boca común de aquellos que vemos sucumbir a nuestros ídolo ante el cansancio de ese extraño síntoma al que llamamos edad, no obstante, cuatro años más tarde volvería a generar una afirmación de esa magnitud, que a la fecha no me ha hecho

quedar mal. Entré por la facultad de ingeniería, como era habitual para cortar camino rumbo a la facultad donde las bancas de madera en la explanada se avistaron. Las puertas corredizas se abrieron para dar paso al pasillo blanco con esas escaleras al fondo, donde no tardaría en abrirse la puerta verde del recinto que asomaba a la cancha de futbol.

El día transcurrió normal, esa primera clase aproveché para mostrarles mis pasiones en esta vida con el uso de una herramienta sofisticada de la teoría de conjuntos, el *Diagrama de Venn*, invitándolos a formar uno y compartieran cada uno el suyo conmigo, tal vez ellos no lo sabían pero con este simple ejercicio se podrían ahorrar semestres de colegiatura en la facultad y no por el hecho de dudar que pudieran culminar sus estudios, seguramente muchos lo harían, sino porque así podrían desenmascarar sus verdaderas pasiones. Encontrar respuesta a esa pregunta tan simple es algo que tarde o temprano llega, ¿O tal vez no?

De espaldas a nosotros el plumón comenzó a dibujar aquello que parecían ser tres círculos sobrepuestos formando algo similar a una flor con tres pétalos. Escribió lentamente en cada uno de los círculos ***Religión, Atletismo*** *y* ***Matemáticas****,* encerró todo en un gran rectángulo con una letra U inscrita en él y en el centro de esa flor a la cual aquel profesor le llamó ***intersección***, señalándola con una voz rasposa dijo —¡Justo ahí me encuentran a mí!, ahora cada uno haga su propio diagrama para poder compartirlo con los demás.

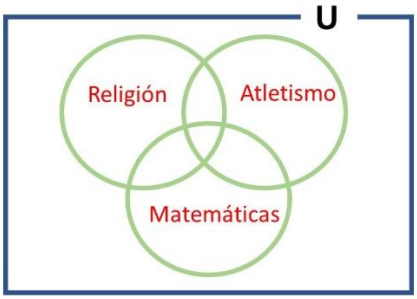

The following story, which the reader may find simple but nevertheless brilliant, will be fundamental to understand the balance of strengths that will be discussed in chapter 2.

There are fundamental facts in this life, things which by nature work that way, this is commonly known as "law", one of many is the conservation of energy. Let's imagine now that we have a little boy named Daniel*, this child has 28 blocks to play with which are indestructible, one day his mother enters his room and only finds 27, but when she looks under the bed she finds the remaining block, the next day she realizes that she finds 26 but when she looks through the open window she finds the remaining two. Something disconcerting happened when one day she found 30 blocks, but it turned out that his friend Gerardo was there and he had taken his two blocks with him.

Well, here the great Feynman explains that energy behaves like those cubes of Daniel, when we see only kinetic energy and something is missing to complete those 27 cubes, it must be out there in potential energy or spring energy, and why not? dissipated in heat. Now, when Gerard comes to play with Daniel and brings his blocks with him, we should not be concerned because some external factor is transferring energy to the system.

And that's how conservation of energy works.

*Feynman calls him "Dennis the Menace."

Chapter 1

Cerium Oxide.

Introduction

Over the last years, trying to find new materials for use in different science fields is not an easy task by two main factors, the completely different features of the material as one parameter such as size, doping-alloy concentration, growth temperature among others is

modified and the extensive number of applications which have emerged nowadays (photovoltaic, catalytic, sensing…).

On this regard, a compound that has taken incredible importance in recent years is cerium oxide (CeO_2), sometimes named just ceria, CeO_2 has been used in a variety of applications for photovoltaic devices traditionally used as an interlayer between Sb_2Se_3 and CdS and in some specific thickness around 3 nm it increases the solar cell efficiency from 2.17% to 5.14% [1], Zhou Xing et al reach a 17.35 % by improving the back contact electronic transport in a perovskite solar cell using a CeO_x film [2], as well a 130 nm film of CeO_2 is employed as a buffer layer in a Bi_2S_3/PbS heterostructure increasing from 0.14% to 1.27% the conversion efficiency [3]. In other applications, CeO_2 works as an electrolyte in Solid Oxide fuel cells (SOFC) reaching a peak power density of 2 W/cm^2 at an operating temperature from 600 °C to 650 °C [4]. In gas sensing, different sensitive elements based on CeO_2 have been used to detect CO_2, NO_2 and CO. Rare earth (RE) doped CeO_2 solid solutions show catalytic activity in CO and $C_6H_5CH_3$ oxidation reactions [5].

The applications mentioned before are possible by a crucial property, its electric conductivity, this electric conductivity has two different contributions, electronic and ionic, the first takes place by carrier transport and the second by the oxygen ions diffusing through vacancies sites [6], ionic conductivity has been a point of interest by different authors because of in CeO_2 and CeO_2 :RE can be separated by two contributions, a grain interior (intragranular) and the grain boundary (intergranular) where the temperature is important to promote this oxygen hopping [7] as well as the concentration of RE ions [6]. The specific concentration which produces a maximal value on ionic conductivity lies between 0.1 and 0.2 for each trivalent ion depending on the synthesis method [8], to understand why occurs this we have to understand a phenomenon that takes place when adding trivalent ions to a CeO_2 lattice, the subsequent generation of oxygen vacancies (OV).

Oxygen vacancies formation

Due to the different oxidation states of Ce, a reduction process from Ce^{4+} to Ce^{3+} always takes place in CeO_x, leading to a subsequent formation of OV in the lattice to maintain the electrical charge. For this reason, it is common to see that this compound is accompanied by Ce^{3+} ions, one way to identify if we have in the lattice either Ce^{3+} or Ce^{4+} bounded with O^{2-} is through the Raman signal for this compound. The Raman spectra for typical CeO_2 consist of a triple degeneracy active mode called F_{2g} formed by one Cerium atom with eight Oxygens surrounding it, the main phonon is located around 460 cm^{-1} and there are other phonons with less intensity around 550 - 600 cm^{-1} [9], [10].

Photovoltaic applications.

In the frame of photovoltaic devices, CeO2 started to be used as a cushion layer increasing considerably its fill factor (*FF*), open circuit voltage (V_{OC}), and short circuit current (I_{SC}) values [3], has also been used for the fabrication of Dye-sensitized solar cells (DSSCs) with different rare-earth dopings such as Europium, where Eu^{3+} nanocrystals promote dual function through Photoluminescence (PL) photoluminescence [11]. The control of Photoluminescence and doping properties are still under study, as well as searching for materials compatible with their properties such as lattice constant, temperature and growth method.

Dielectric function and F-centers.

The electrical properties of CeO_2 have also been studied extensively, Patsalas et al. have used a double Tauc-Lorentz model to study the dielectric function, they found a beautiful relation between the density and the refractive index, discussing the Gd_2O_3, Ce_2O_3 domains and their relation with the *4f* and *5d* levels [12]. Other authors have studied the emission by defects within the *4f* state, namely F-Centers [13], these defects are still being

studied, and recently, well-defined emissions have been found using micro photoluminescence [14].

Magnetic properties.

Regarding the magnetic properties of the material, only few studies have been done on CeO_2 films, doped with certain materials such as cobalt [15]. On the other hand, it is well known that gadolinium has a ferromagnetic nature, and studies of the properties of Gd-doped CeO_2 thin films are scarce [16].

Chapter 2

Theoretical Frame

Homogeneous Deformation.

To discuss the influence of homogeneous stress on the electronic energy levels, we will first try to understand how they work in a semiconductor with a Zincblende structure and then we will try to adapt it to the characteristic structure for CeO_2, which has Fluoruite-type structure with a triple degeneracy. Both structures are face-centered cubic (fcc), the difference lies in the fact that in the first one, there is a subcube where only 4 of the vertices are occupied by ions, while in the Cerium lattice the eight vertices of the cube are occupied by ions.

In the absence of strain or spin-orbit splitting the valence-band edge at k=0 in zincblende material is a sixfold multiplet with orbital symmetry Γ_{15}. The spin-orbit interaction lifts this degeneracy into a fourfold degenerate (including spin) $P_{3/2}$multiplet (J = 3/2, M_J=$\pm 3/2 , \pm 1/2$ and a $P_{1/2}$ (J = 1/2, M_J=$\pm 1/2$) in spherical notation (Figure 1)

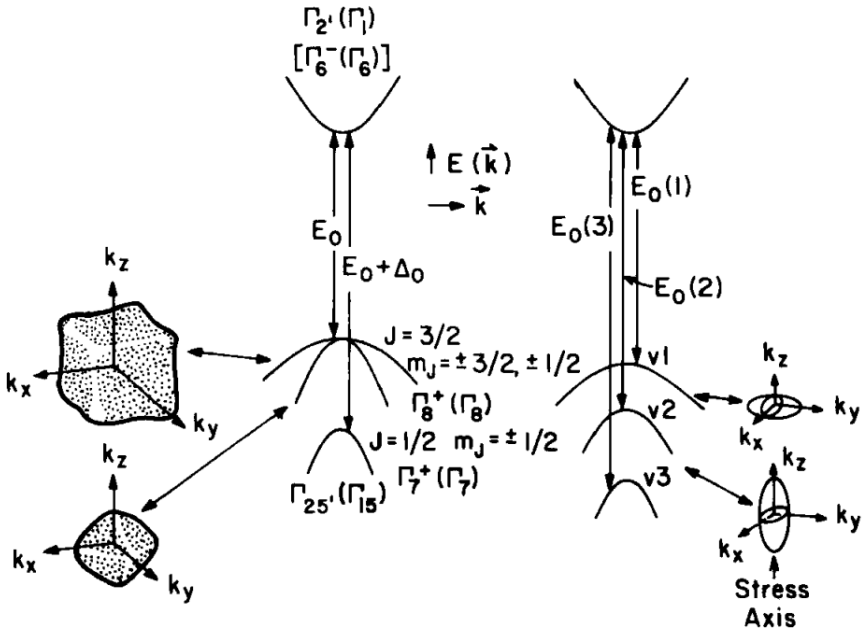

Figure 2.1. Valence bands (J = 3/2, M_J=$\pm 3/2 , \pm 1/2$ and a $P_{1/2}$ J = 1/2, M_J=$\pm 1/2$) and lowest conduction band [r2,(r1)] in diamond- and zincblende-type semiconductors for unstrained (left-band) and strained (right-band.

The fundamental direct gap is the energy difference between Γ_6^- (Γ_6) and Γ_8^- (Γ_8), conduction and valence bands, denoted as E_0. The spin orbit splitting is Δ_0 and $\Delta_0 + E_0$ is the transition energy between Γ_6^- (Γ_6) and spin orbit splitting Γ_7^- (Γ_7) . A strain with a uniaxial component splits the J = 3/2 multiplet into a pair of degenerate Kramers doublets (right side in Figure 1). The three valence bands are labeled v1, v2, and v3.

The total Hamiltonian for a system like this can be written as:

$$H = H_k + H_{so} + H_\varepsilon^{(c)} + H_\varepsilon^{(1)} + H_\varepsilon^{(2)} \quad (2.1)$$

Where H_k is the $\boldsymbol{k} \cdot \boldsymbol{p}$ perturbation approach, H_{so} is the spin-orbit interaction and $H_\varepsilon^{(1)} + H_\varepsilon^{(2)}$ are the orbital-strain Hamiltonian and the strain-dependent spin-orbit Hamiltonian which depends on the deformation potentials (a , b , d).

For wave functions that make H_{so} diagonal, functions with the same transformation properties as the eigenfunctions of the total angular momentum operator J(= L+S) i.e $\left[J, M_J\right\rangle$ with Lowdin's class and considerations of perturbation theory, The Hamiltonian matrix can then be written in a 8x8 matrix which at k=0 for a strain with a uniaxial component along [001] or [111] it reduces to

$$\begin{bmatrix} E_0 + \delta E_{H,c}^m & 0 & 0 & 0 \\ 0 & \delta E_{H,v}^m - \delta E_S^m & 0 & 0 \\ 0 & 0 & -\delta E_{H,v}^m + \delta E_S^m & \sqrt{2}\,(\delta E_S')^m \\ 0 & 0 & \sqrt{2}\,(\delta E_S') & -\Delta_0 - (\delta E_{H,v}')^m \end{bmatrix} \quad (2.2)$$

For the strained layers superlattices, the more relevant situation is for biaxial strain, ε, in the (001), (111) and (011) planes. In the former two cases the equation (2.2) remains the same with

$\delta E_{H,c} = a_c\,(2 - \lambda^m)\,\varepsilon$,

$\delta E_{H,v} = (a_1 + a_2)\,(2 - \lambda^m)\varepsilon = a\,(2 - \lambda^m)\,\varepsilon$

$$\delta E'_{H,v} = (a_1 - 2a_2)(2 - \lambda^m)\varepsilon = a'(2 - \lambda^m)\,\varepsilon$$

$$\delta E_S^{(001)} = -(b_1 + 2b_2)[1 + \lambda^{(001)}]\,\varepsilon = -b\,[1 + \lambda^{(001)}]\,\varepsilon \qquad (2.3)$$

$$(\delta E')_S^{(001)} = (b_1 - b_2)[1 + \lambda^{(001)}]\,\varepsilon = -b'\,[1 + \lambda^{(001)}]\,\varepsilon$$

$$(\delta E)_S^{(111)} = -[(d_1 + 2d_2)/2\sqrt{3}][1 + \lambda^{(111)}]\,\varepsilon = -(d/2\sqrt{3})[1 + \lambda^{(111)}]\,\varepsilon$$

$$(\delta E')_S^{(111)} = -[(d_1 - d_2)/2\sqrt{3}][1 + \lambda^{(111)}]\,\varepsilon = -(d'/2\sqrt{3})[1 + \lambda^{(111)}]\,\varepsilon$$

with

$$\lambda^{(001)} = 2C_{12}/C_{11} \qquad (2.4)$$

$$\lambda^{(111)} = 2(C_{11} + 2C_{12} - 2C_{44})/(C_{11} + 2C_{12} + 4C_{44})$$

Where a and a' are interband hydrostatic deformation potentials, ε is the in-plane strain, and the C_{ij} are the elastic stiffness constants, then the effect of strain is to create a hydrostatic shift and split the degeneracy in $\mathbf{v_1}$ and $\mathbf{v_2}$ like in Figure 1.

It is important to point out that the monitoring of the transitions E_0 , E_0+ Δ_0 as well as the splitting of $\mathbf{v_1}$ and $\mathbf{v_2}$ is possible using techniques such as photoreflectance, electroreflectance and photoluminescence. Two things are important here, the nature of the band structure of the material and the instrumentation used to observe such transitions. In general, three important aspects must be considered: the energy of the incident beam, the proper polarization and the control of the stress applied in the desired direction.

The band structure of CeO_2 is somewhat complex as pointed out in the introduction, so the deformation potentials for this material have not been studied. However, the elastic constants for the material are known theoretically as Tanju and Resul report them as C_{11}= 386 C_{12}= 124 C_{44}=73 [17].

These values play an important role when we start talking about the dielectric function.

.

Homogeneous deformation on $q \approx 0$ Optical phonons

Since at $q \approx 0$ the CeO_2 phonon has Γ_{25}' (Γ_{15}) symmetry, to understand the effects of strain on its main F_{2g} phonon [9] the case of a Diamond-Zincblende structure will be presented first, for this reason, the first section was crucial because of we can use the same approach (i.e. electronic valence bands at k=0) for Raman-active phonons ($q \approx 0$ optical phonons).

In this case the Hamiltonian has as the following expression

$$H_\varepsilon = [(p+2q)/6\omega_0]\left(\varepsilon_{xx}+\varepsilon_{yy}+\varepsilon_{zz}\right)$$
$$-[(p-q)/(2\omega_0)]\left[\left(L_x^2-\tfrac{1}{3}L^2\right)\varepsilon_{xx}+cp\right] \quad (2.5)$$
$$-(r/\omega_0)\,[(L_xL_y+L_yL_x)\varepsilon_{xx}+cp\,]$$

Where *p*, *q* and *r* are deformation potentials that describe the changes in the "spring constants" at $q \approx 0$ ($\vec{k} \approx 0$) optical phonons with strain, the quantity $(p+2q)/6\omega_0 = -\gamma$ is called the mode Grüneisen parameter and came from the shift due the hydrostatic component of the strain [18]

As mentioned Cardeira et al., in absence of stress, the first-order Stokes-Raman spectrum of a diamond-type material exhibits a single peak at $q \approx 0$ which is a single triple degenerated optical phonon (F_{2g}, Γ_{25}') [19].

Diamond-Type Material.

In this case the Hamiltonian :

$$H = \omega_0 + H_\varepsilon \quad (2.6)$$

And using the Γ_{25}' and the wave functions for X, Y and Z this Hamiltonian can be written in a 3x3 matrix and for uniaxial strain along [001] or [111] directions, the matrix can be easily diagonalized, and we have two cases:

- The threefold degenerated of the $q \approx 0$ optical phonon is split into a singlet with eigenvector parallel to the strain axis (Ω_s)
- A doublet with eigenvector located in the plane perpendicular to the strain axis (Ω_d).

Fort these two cases the wavenumber of the phonon is given by:

$$\Omega_s = \omega_0 + \Delta\Omega_H + (2/3)\Delta\Omega_s$$

$$\Omega_d = \Omega_0 + \Delta\Omega_H - (1/3)\Delta\Omega_s \quad (2.7)$$

And the expressions for $\Delta\Omega_H$ and $\Delta\Omega_S$ in the case of an external stress **T** ll [001] and **T** ll [111] have been given in [19],[20].

For these situations in which we have an in-plain strain (ε) either (001) or (111) planes, we have:

(001) strain

$$\Delta\Omega_H^{001} = [((p + 2q)/6\omega_0)][2 - \lambda^{(001)}]\varepsilon$$

$$\Delta\Omega_{S}^{001} = [((p + 2q)/6\omega_0)][1 + \lambda^{(001)}]\varepsilon \qquad (2.8)$$

(111) strain

$$\Delta\Omega_{H}^{111} = [((p + 2q)/6\omega_0)][2 - \lambda^{(111)}]\varepsilon$$

$$\Delta\Omega_{S}^{111} = [(r/\omega_0)][1 + \lambda^{(111)}]\varepsilon \qquad (2.9)$$

Where $\lambda^{(001)}$ and $\lambda^{(111)}$ were given in (2.4).

For CeO_2 the triple degeneracy is known from experimental [21] and theoretical [9] [17] results,

Experimentally, no reports have been found on how the phonon dispersion curves (PDC) behave for this material under applied stress. In Figure 2.2 we can see the PDC for different gadolinium concentrations which were obtained based on the results of Swanand et al. for CeO_2 doped with Neodymium (Nd) and Lanthanide (Ln).

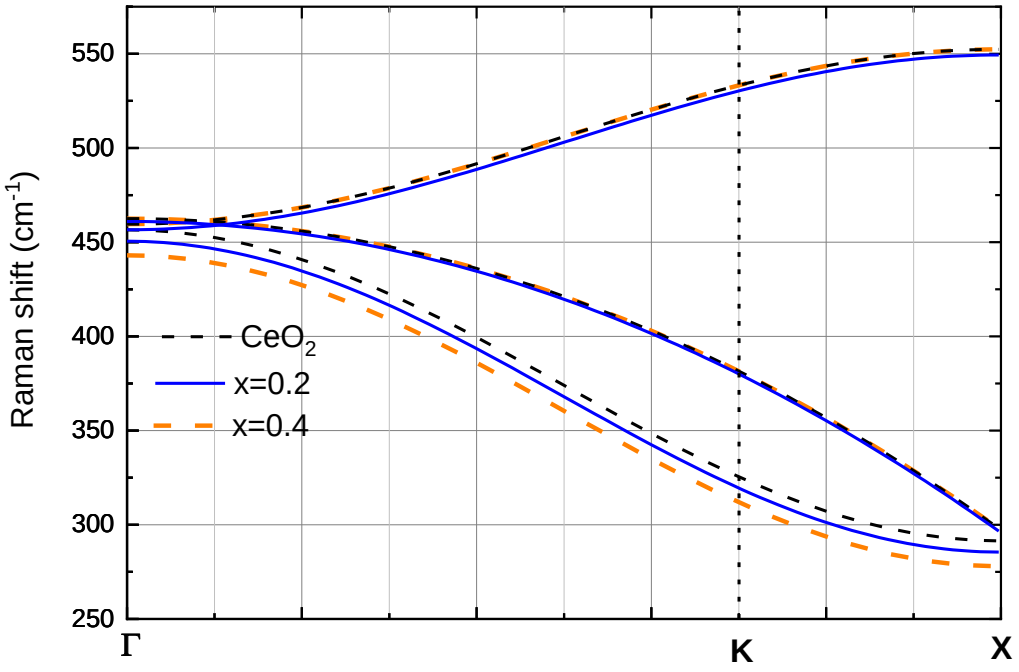

Figure 2.2. Phonon dispersion curves (PDC) for CeO_2 with different Gd concentrations

The results are summarized in Table 1. It should be noted here that trying to follow the F2g mode from the spatial correlation model using equation 2.10 was not only possible by varying the correlation length ***L*** and the full width half maximum (FWHM) $\boldsymbol{\Gamma_0}$, it was also necessary to

$$I(\omega) = \int e^{\left(\frac{-qL^2}{4}\right)} \frac{d^3q}{\omega - \omega(q) + (\Gamma_0)} \qquad (2.10)$$

modify the PDC (***B1***,***B2*** and ***B3*** in Table 1.), which gives us an idea that some Strain is affecting the lattice and that it comes from the gadolinium incorporation.

Table 1. PDC (***B1, B2, B3***) obtained for CeO_2:Gd in glass substrates and parameter for the correlation length and FWHM.

Gd concentration(X)	*L (Å)*	Γ_0(cm^{-1})	*B1,B2,B3*
0	45	18	506 -46.4cos(πq) 462.5- [165.2(q^2)] 374+[82.5*cos(πq)]
0.2	24	18	503 -46.4cos(πq) 461- [165.2(q^2)] 368+[82.5*cos(πq)]
0.4	15	35	506 -46.4cos(πq) 462.5- [165.2(q^2)] 360.5+[82.5*cos(πq)]

With this last consideration it was possible to obtain the fit of Figure 3. using 2.10 for the F_{2g} mode, and this helps us to understand that somehow for the CeO_2:Gd spin-orbital interactions are taking place due to the strain either coming from the substrate or by OV, and that deformation potentials (*p,q*) could be obtained in this system with samples that present better growth properties.

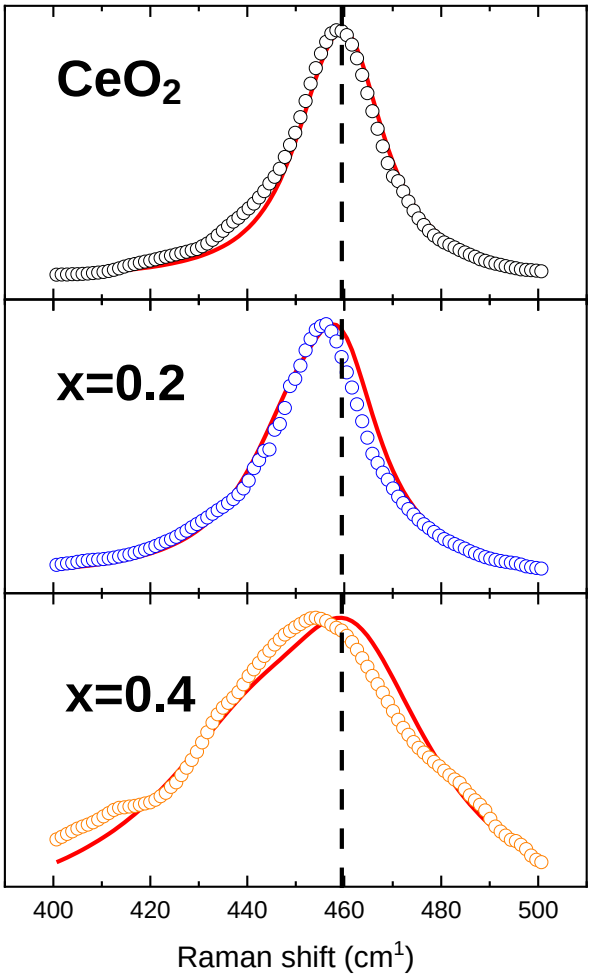

Figure 2.3. F_{2g} mode for different Gd concentrations, in solid red line the fit using eq 2.10 from Γ to K along ***B1***,***B2*** and ***B3.***

A brief story of strain in crystals

Now we shall consider that a phonon is observed under an applied strength, we call to this strength a *perturbation*, there are several factors that can shift this phonon either to low or high wavenumbers (i.e., the lattice can be perturbed in different ways) and this may be by temperature (*latt*), substituting atoms of other compound (*bond*), applying a certain pressure (*press*), anharmonic processes that may take place (*anh*), among other factors.

Now let's examine this situation in terms of newton's first law, if we only had *inertia* and tried to observe the phonon as a function of any of the factors mentioned above, the result would be something like that shown in Figure 2.4. where for practical purposes we denote the perturbation as X and $\boldsymbol{\omega_0}$ represents the wavenumber of the phonon

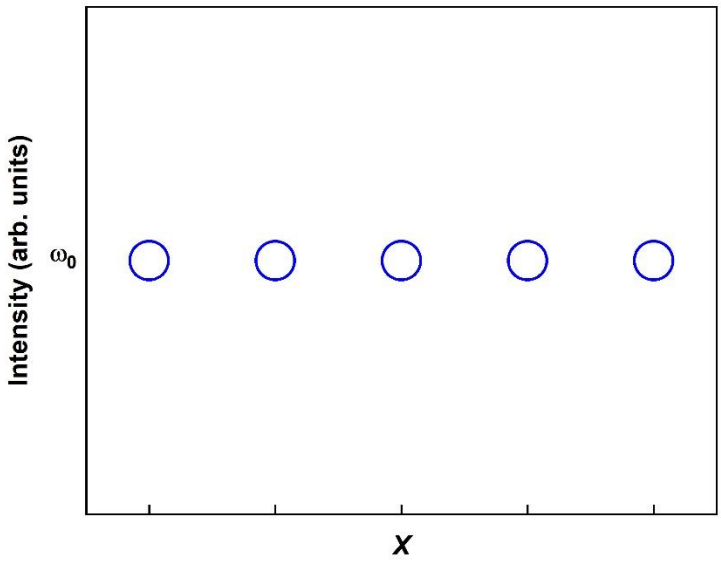

Figure 2.4. Phonon without any external strength, ω_0 denotes the wave number and X is a perturbation.

Now we must remember Daniel's brief story, but this time we will imagine that instead of blocks he has a field hockey puck with different ropes tied and assigned with the numbers strictly as shown in Figure 2.5, for practical purposes we will assume that Daniel can move the puck only in the direction in which the ropes are drawn and that his mother every day returns the puck to the same position.

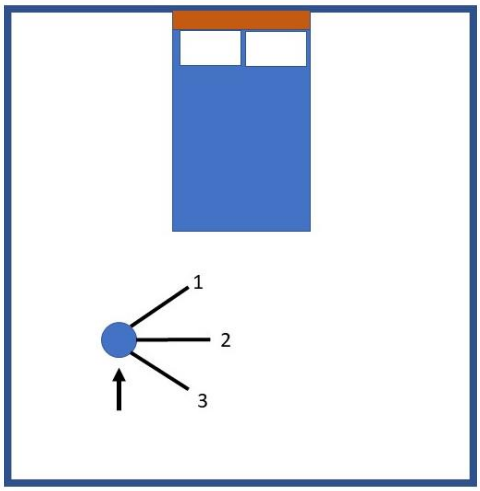

Figure 2.5. Daniel's room, the ropes (assigned with numbers from one to three) can pull the puck strictly in the direction indicated, the arrow is only a reference position.

During the whole day he likes to play at dragging the puck around his room. When his mother enters the room just as she sends him to sleep, she notices that the puck is in the position it was in the morning (indicated as an arrow), so his mother assumes that he did not pull any of the strings. Hence, we have the case of Figure 2.4.

On another day, something different happened, the mother found the field puck in the position shown in Figure 2.6, and quickly realized that Daniel only played with the rope 1

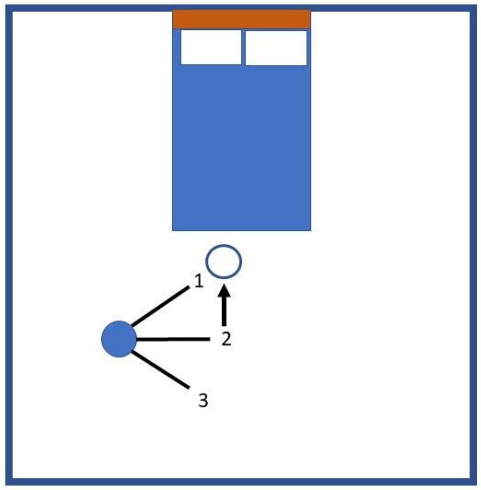

Figure 2.6. Daniel's room, pulling just the rope 1.

After a week, his mother entered the room six times at different hours during the day (Denoted with Roman numerals) and noticed how the puck changed its position in the room, which can be seen in Figure 2.7.

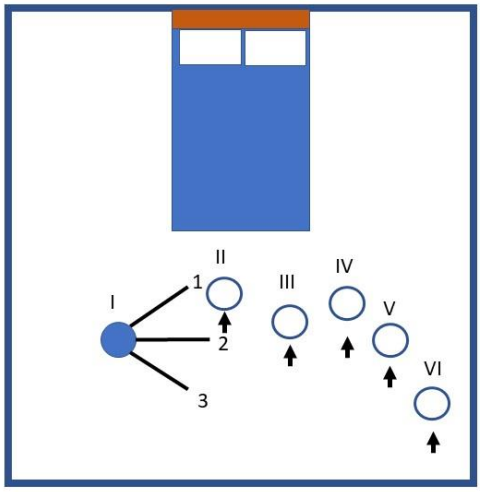

Figure 2.7. Daniel's room at six different times of the day.

Here, the situation becomes somewhat complicated, because for Daniel's mom it is not so evident which rope he pulled first, or the order in which he did it. For example, to get to case II, he could have first pulled string 3 a little and then pull rope 1, or he could have pulled string 2 and then pull rope 1.

Something that could be evident to the mother, for example, is that for case VI Daniel must have used string 3, otherwise with 1 and 2 it would be impossible to reach this *state*.

If we would now see Daniel's room in an image like Figure 2.4, we will get the following case, where the position of the puck in the course of the day will be visualized as in Figure 2.8.

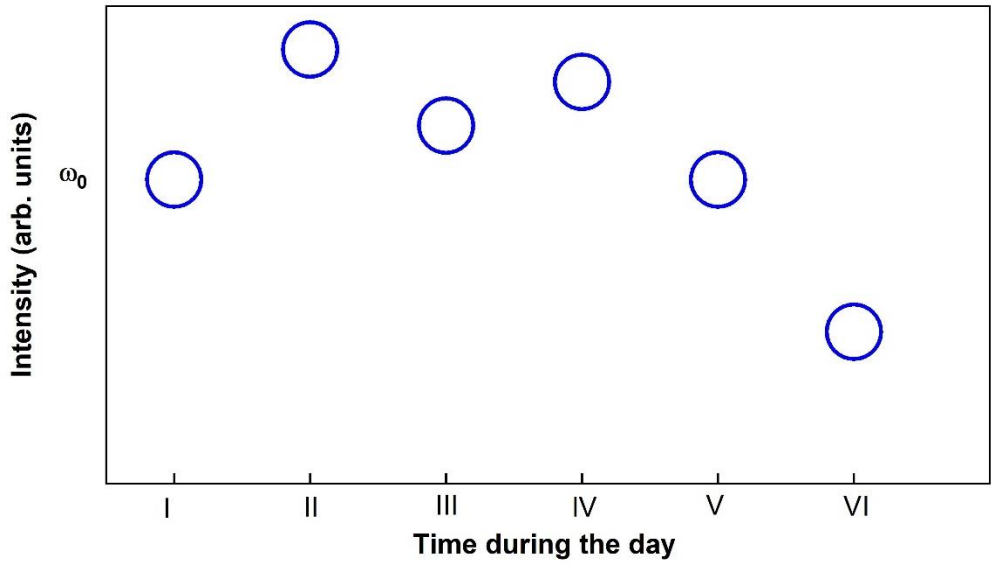

Figure 2.8. Position of the disc observed by the mother during the course of the day.

Now let's do the following:

We shall assign a *perturbation* to each rope, we will call rope 1 temperature ($\Delta\omega_{latt}$), the second rope anharmonic processes ($\Delta\omega_{anh}$) and the last one pressure ($\Delta\omega_{press}$).

Thus, considering the initial position of the puck we would have the following equation.

$$\Delta\omega = \Delta\omega_{latt} + \Delta\omega_{anh} + \Delta\omega_{press} \quad (2.5)$$

Where $\Delta\omega$ is the sum of all contributions (the experimental way that we see the phonon).

Normally in practice, depending on the material and phonon we want to study, we will restrict the number of perturbations we have, some will be intrinsic to the material while others will be externally influenced and other are just negligible, but Daniel's mom's goal will always be to find out which ropes he pulled, the order in which he did it, if he pulled two at the same time, which one he pulled more. However, she has to find the last point where the puck was left at the end of the day.

In the CeO_2 case it turns out that we have the following expression.

$$\Delta\omega = \Delta\omega_{strain} + \Delta\omega_{bond} \quad (2.6)$$

Where $\Delta\omega_{strain}$ if you keep reading these lines will be interpreted as a *strain* that is caused by the substrate and an OV contribution.

Finally, to conclude this new story, remembering that Daniel's blocks satisfy the conservation of energy, could it be demonstrated that a phonon and its perturbations also satisfy it?.

For this it is enough to remember that a phonon comes from the excitation of a base state to another by means of a specific beam ($h\upsilon_f$ - $h\upsilon_i$), only seen in terms of wave numbers (cm^{-1}), but that does not imply that it is not energy! Therefore, *we say that booth stories are the same just from different point of views.* QED

Dielectric function of the material.

A variety of models have been proposed to get a reliable fit of the real and imaginary part of the dielectric function, some of them are useful depending on the behavior of the material, if it is absorbing, semi-transparent or metal. In most of the cases the fitting parameters used in the model are chosen because of their physical meaning, or they are related with constants which have a physical meaning such as the energy gap E_g, the plasma frequency ω_p equivalent to $\sqrt{n_e e^2/m^* \varepsilon_0}$, where n_e is the carrier concentration, e the charge of the electron, m^* the effective mass and ε_0 the vacuum permittivity. And another important fact is that any model must have Kramers- Kronig consistency, it means once the real or imaginary part has been found the other one can be inferred.

Among the different models the Tauc-Lorentz dispersion, which involves Tauc's joint density of states and Lorentz's oscillator, works very well for dielectric amorphous or polycrystalline materials.

Tauc-Lorentz model

$$\varepsilon_2 = \frac{AE_0\Gamma(E-E_g)^2}{(E^2-E_0)^2+\Gamma^2E^2}\frac{1}{E}\ ,\ E > E_g$$

$$\varepsilon_2 = 0\ ,\ E \leq E_g$$

And the real part is obtained by the Kramers-Kronig integration

$$\varepsilon_1 = \varepsilon_\infty + \frac{2}{\pi}P\int_{E_g}^{\infty}\frac{\xi\varepsilon_2(\xi)}{\xi^2-E^2}d\xi$$

Where ε_∞ represent the contribution of optical transitions at higher energies and appears as an additional parameter.

B-Spline model

The B-spline of degree 0 is defined by

$$B_i^0(x) = \begin{cases} -1 & t_i \leq x < t \\ 0 & otherwise \end{cases}$$

The higher degree B splines are defined by a *recursive* definition

$$B_i^k(x) = \left(\frac{x - t_i}{t_{i-k} - t_i}\right) B_i^k(x) + \left(\frac{t_{i+k+1} - x}{t_{i+k+1} - t_{i+1}}\right) B_{i+1}^{k-1}(x) \quad (k \geqq 1)$$

To demonstrate that this expression is valid Cheney and Kincaid use induction to demonstrate that is valid [22][23], as well the Kramers-kroning consistency is well known. But here we have to remark that there are cases in which the induction is false even when it seems to be mathematically consistent (it is like throwing a domino chain by pulling from the second one, but the first one never fell).

In general, with ellipsometric models the same thing can happen, in the case where the number of knots or Tauc-Lorentz blocks are too many and the model parameters do not provide a valid physical interpretation.

Anisotropies

It is well known that there is a distinction between materials according to the way in which their domains are arranged and they are usually assigned to one of the following three sets: amorphous, polycrystalline and crystalline.

When a material is crystalline with preferred orientation and rotatation, we can see a different plane with a different chain of atoms, we could say that the material is *anisotropic*. On the other hand, if we have a polycrystalline material in which its domains have different orientations (i.e. there is no distinction in reflectivity in seeing an average) and when rotating it azimuthally the chain of atoms is the same, we will call it *isotropic*. Note here that the nature of materials is so complex because of it could happen that the same material has certain domains that make it appear anisotropic and when observed in another region it would give the impression that it is isotropic.

To better explain the word anisotropy we will use Figure 2.9 and the Reflectance Anisotropy Spectroscopy (RAS) technique, note that in Figure 2.9 a), by rotating 90° with respect to the red line (0°) we find the same chain of atoms in both directions and after subtracting the reflectivity, the signal is cancelled, i.e. there is no anisotropy, while in Figure 2.9 b) when rotating 90°, the incident light gives us a different reflectivity, in other words we would obtain a signal due to the different chain of atoms, in this case we have an anisotropy.

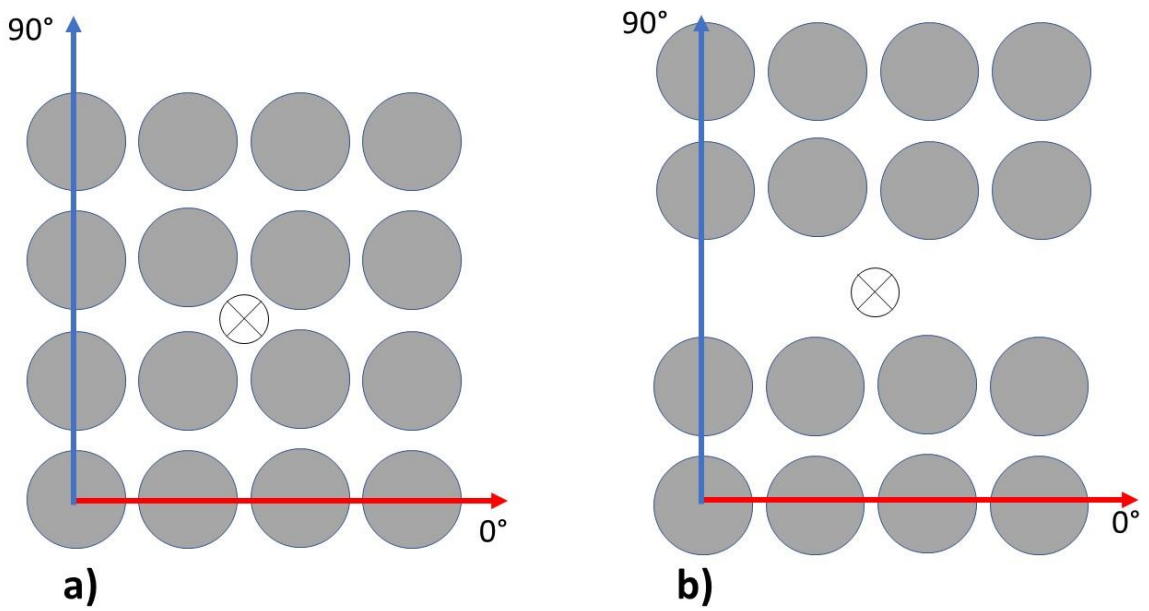

Figure 2.9. Diagram for a) Isotropic case, b) anisotropy observed considering RAS signal rotating from 0° to 90° in an azimuthal direction the cross circle indicate the direction of the polarized electromagnetic wave.

RAS and SE have much in common despite having a different instrumentation, while for ellipsometry a specific angle of incidence is used, RAS is almost at normal incidence, this allows the possibility that by using the dielectric tensor we can fit the RAS signal. From the propagation of light through several media, considering the phase change, it is possible to get the complex reflectivity r using the following equation [24].

$$r = \frac{r_{01} + r_{12}\, e^{-2i\delta_1 \ldots}}{1 + r_{01} r_{12} e^{-2i\delta_1 \ldots}} \quad (2.7)$$

Where r_{ij}=$(n_i - n_j)/(n_i + n_j)$ is the complex reflection coefficient at the interface between the *i* and *j* media at normal incidence, δ_i is the phase factor given by $\delta_i = 2\pi n_i d_i/\lambda$, here n_i, d_i and λ are the refractive index , the thickness of the film and the wavelength respectively.

Using this reflectivity and the values obtained from the ellipsometric model, it is possible to obtain RAS using equation (2.8), even to see and understand strain effects in heterostructures below the Gap.

$$\frac{\Delta r}{r} = A\frac{2\pi d_1}{\lambda}\frac{1}{r}\frac{\partial r}{\partial \delta_i}\Delta n_1 + B\frac{r_{12}}{r}\frac{\partial r}{\partial r_{12}}\frac{\Delta r_{12}}{r_{12}} \quad (2.8)$$

Magneto-Optic effect.

When light interacts with a material in the presence of a magnetic field, interesting phenomena can occur according to the nature of the material, i.e. whether it is magnetic, ferromagnetic or paramagnetic.

Among the ferromagnetic materials, those whose domains can be rearranged in the presence of a magnetic field are Gadolinium and CeO_2 when working with valence number 3+.[25] [26] [27].

Light-matter interaction in the presence of a magnetic field is complex for several reasons, including whether the material is anisotropic or isotropic. In general, 3 different configurations have been distinguished for the direction of the magnetization vector $\vec{\mathrm{M}}$= $\boldsymbol{M_x} + \boldsymbol{M_y} + \boldsymbol{M_z}$, ($\boldsymbol{M_x} = \mathbf{M}\sin\varphi cos\gamma\ \boldsymbol{M_y} = \mathbf{M}\sin\varphi sin\gamma\ \boldsymbol{M_x} = \mathbf{M}\, cos\gamma$) and the plane of incidence in spherical coordinates as shown in Figure 2.10.

- Polar $\varphi = 0$

- Longitudinal $\varphi = \pi/2 \ \gamma = \pi/2$

- Transversal $\varphi = \pi/2 \ \gamma = 0$

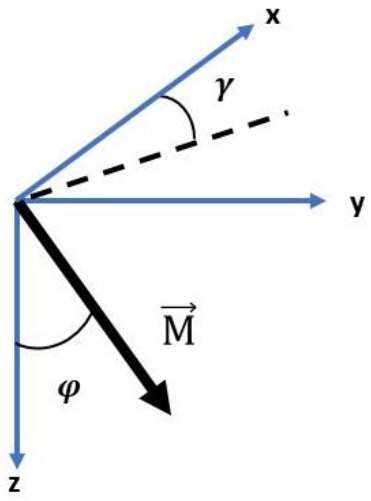

Figure 2.10. Magnetization direction in spherical coordinates as in ref [28] .

Recently, Kerr rotation and Ellipticity have been studied for different magnetization configurations, J. Zak, E. R. Moog, C. Liu and S.D. Bader have succeeded in reducing the analysis to 2x2 matrices, facilitating the study of more specialized heterostructures [28]

[29] . However, we are interested in the use of this theory for applying it in RAS measurements made on CeO_2:Gd/ Si(001) samples.

Starting with the magnetic field and electric field vectors

$$F = \begin{bmatrix} E_x \\ E_y \\ H_x \\ H_y \end{bmatrix} P = \begin{bmatrix} E_s^{(i)} \\ E_p^{(i)} \\ E_s^{(r)} \\ E_p^{(r)} \end{bmatrix} \quad (2.9)$$

Where $E_s^{(i)}$ and $E_p^{(r)}$ are the perpendicular and parallel electric field components respectively, and (i), (r) denote the incident and reflected waves, the medium boundary matrix A is defined by $F = AP$ that for two media, the following relation can be made $A_1P_1 = A_2P_2$, J. Zak et al solve the problem of wave propagation in a magnetic field with this A matrix and boundary propagation matrix $\overline{D}$. For a specific magnetization $\overrightarrow{\mathrm{M}}$ in a polar configuration, the dielectric tensor ε is given by.

$$\varepsilon = N^2 \begin{bmatrix} \mathbf{1} & iQ & \mathbf{0} \\ -iQ & \mathbf{1} & \mathbf{0} \\ \mathbf{0} & \mathbf{0} & \mathbf{1} \end{bmatrix} \quad (2.10)$$

Here Q is the Voight parameter and there are different ways to obtain it [30].Following this approach J. Zak et al. use this A and $\overline{D}$ matrixes which already contemplate the change of sign due to the presence of a magnetic field in multilayers. From equation 6 in reference [29], one may write $P_i = MP_f$ where *M* is given by:

$$M = A_i^{-1} \prod_m A_m \ \overline{D}_m \ A_m^{-1} \ A_f \equiv \begin{bmatrix} G & H \\ I & J \end{bmatrix} (2.11)$$

In this expression ***G***, ***H***, ***J*** and ***I*** are 2x2 matrixes and it can be shown that [29]

$$\begin{bmatrix} t_{ss} & t_{sp} \\ t_{ps} & t_{pp} \end{bmatrix} = G^{-1}$$

$$\begin{bmatrix} r_{ss} & t_{sp} \\ r_{ps} & t_{pp} \end{bmatrix} = IG^{-1} \qquad (2.12)$$

Where r and t are the magneto-optical transmission and reflection coefficients, which we can obtain Kerr- Rotation ϕ' and ellipticity ϕ'' that for s and p polarizations we have:

$$\phi'_p + i\phi''_p = \frac{r_{ps}}{r_{ss}}$$

$$\phi'_s + i\phi''_s = \frac{r_{sp}}{r_{pp}} \quad (2.13)$$

It is possible to adapt this formalism (from the contour and propagation matrices) by solving them numerically and with the help of SE.

For that we must have the following considerations and the correct experimental data.

The angle must be set to 5°, which is particular for RAS.

The main diagonal of equation 2.10 is the dielectric tensor if the material is isotropic, from the model used in SE one can obtain the dielectric function of both the material and the substrate (i.e. n and k).

The range in electronvolts (eV) will also be given by the selected range in RAS and SE.

The Voigt parameter, which is also a complex parameter, will be obtained by SE in the presence of a magnetic field in polar configuration as in [31].

The program developed in Matlab can be found in Appendix I.

Chapter 3

EXPERIMENTAL SECTION

Samples preparation.

The CeO_2:Gd thin films were prepared by a spin coating process starting with a solution precursor made as follows:

Cerium(lll) Chloride heptahydrate ($Cl_3Ce \bullet 7H_2O$)(0.2M) and citric acid (0.2) were mixed in methanol, after 5 min under stirring Gadolinium (lll) Chloride hexahydrate ($Cl_3Gd \bullet 6H_2O$) (0.2M) was added in a x concentration to get $Ce_{1-x}Gd_xO_{2-x/2}$ (x=0.0006, 0.00125, 0.0025, 0.005, 0.01, 0.05, 0.1, 0.2, 0.3, 0.4). The final solution was sonicated for 1h at 50°C, 37kHz – 70 W and finally left at room temperature for 24 h.

The films were deposited on glass, Sn_2O:F commercial glass slides substrates (TCO), and Silicon(001) substrates, by adding 90 μl in a 3 stages dynamic deposition program, 15 s at 100 rpm, 30 s at 2500 rpm and 15s at 100 rpm. At the end of the deposition the samples were heated on a heating plate for 10 min at 90 °C or 270 °C, this process was repeated 5 times for all samples followed by a final annealing in air at 550 °C for 5 h.

The Sb_2S_3 thin films were prepared by chemical bath deposition according to the procedure reported by Bindu et al. [14], 650 mg of antimony trichloride ($SbCl_3$) were dissolved in 2.5 ml of acetone, in a 100 ml beaker. Subsequently, 25 ml of 1 M sodium thiosulfate ($Na_2S_2O_3$) were added followed by 75 ml of water, introduced vertically into the beaker and the solution was kept at 10°C for a deposit period of 2h.

P-type B-doped Si was deposited in a radio-frequency planar magnetron sputtering system with a base pressure under 10^{-4} Pa. Two independent Ar (99.999%) glow discharges were maintained to pulverize two 7.5 cm water cooled Si:B and Si (99.999%) targets at a sputtering pressure of 1 Pa. The substrates were fixed to a molybdenum block, which was placed 5 mm under a BN heater, with a target substrate separation of 5 cm. An

applied power of 200 W and a substrate temperature of 500°C was used in the sputtering experiments.

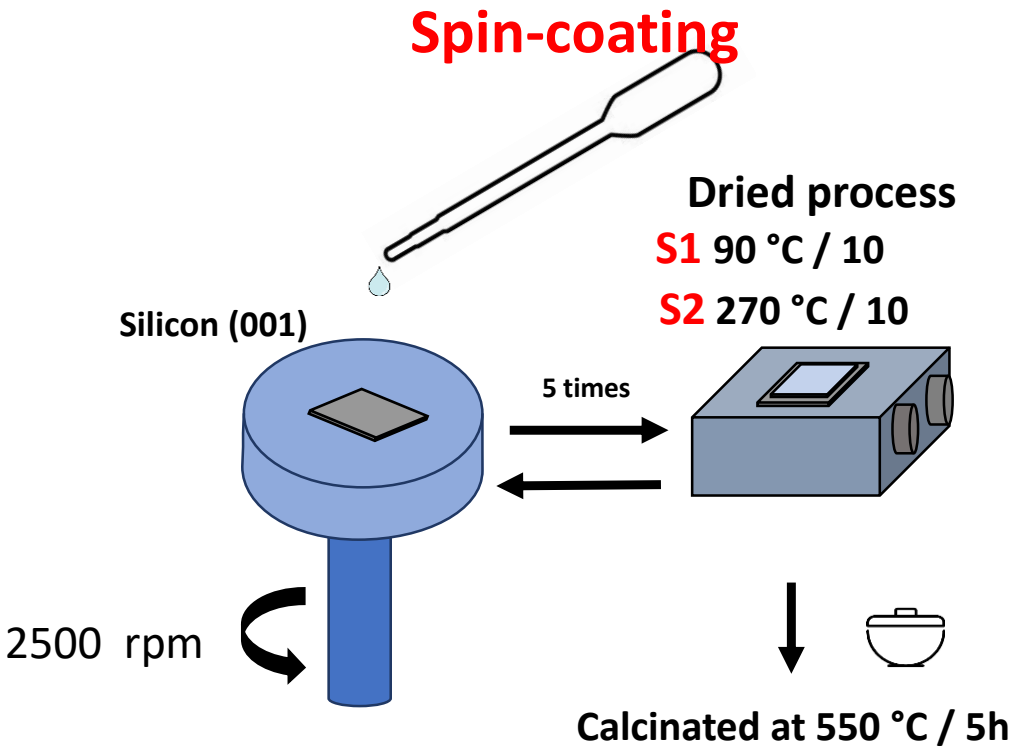

Figure 3.1 Spin-coating process

Fabrication of the p-n junction

The diode heterostructures were made depositing CeO_2:Gd, as the n-type layer, on TCO substrates. Afterwards, p-type Sb_2S_3 or Si thin films were deposited on CeO_2 and graphite paint was applied on the sample surface with a subsequent layer of silver paint as

electrical contact. Thus, the obtained device heterostructures are TCO/CeO2:Gd/Sb_2S_3/graphite/Ag (H1) and TCO/CeO2:Gd/Si:B/graphite/Ag (H2) displayed in Figure 3.2.

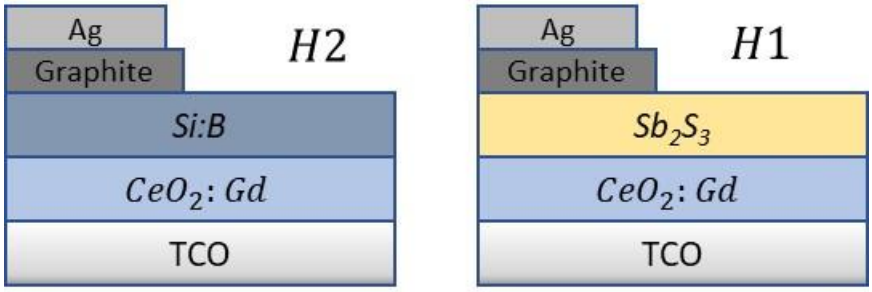

Figure 3.2. p-n heterostructures for TCO/CeO2:Gd/Sb_2S_3/graphite/Ag (H1) and TCO/CeO_2:Gd/Si:B/graphite/Ag (H2).

The Raman spectra of the thin films were measured with a Horiba XploRA Plus microscope at room temperature using a 532 nm DPSS laser through a 100X objective for an effective 1 mW power on the sample surface. The spectra were acquired with a 2400 grooves/mm grating and thermoelectrically cooled CCD for 20 s in 3 accumulations. The X ray diffraction (XRD) curves were measured using a Panalytical Empyrean diffractometer with a Cu anode operating at 40 kV–30 mA in a grazing incidence (0.5◦ incidence angle) configuration. Spectroscopic ellipsometry (SE) measurements were carried out with two ellipsometers an Horiba (from 0.6 eV – 4.75) and a Woollam (from 0.734 to 6.477). Scanning electron microscopy (SEM) images were acquired by a FEI-Inspect F50 microscope using 30 kV of acceleration voltage. Hall mobility and carrier concentrations were determined using an Ecopia HMS-3000 system at 0.17 T in the van der Pauw configuration. The Current-Voltage measurements were carried out using a Keithley equipment under AM1.5 illumination.

Chapter 4

RESULTS AND DISCUSSION

This chapter presents the results regarding the analysis of the CeO_2:Gd films grown onto glass and Silicon (001) substrates. The evolution of the Raman spectra as a function of the temperature is discussed as well as the starting temperature formation of the polycrystalline phase found by temperature-Raman measurements, nevertheless, differences between the two phases CeO_2 and Gd_2O_3 are not evident by using XRD and only a change in the lattice parameter takes place. This expansion is used to understand the strengths of the lattice which were divided in two main components, *strain* and *bonding* from which the behavior of the dielectric function was treated to be understood. Finally, a device was fabricated to demonstrate the n-type nature of the material and the analysis is shown in this chapter.

XRD and in situ Raman measurements for CeO_2:Gd films.

One of the most common issues in CeO_2:Gd system arises from the complications of identifying the Gd_2O_3 phase from XDR patterns, this compound has a lattice parameter of 1.08 nm the double of CeO_2 lattice parameter (0.541 nm). In Figure 4.1 the XRD patterns for films grown on glass substrates with different Gd concentrations are shown, the peaks correspond to the cubic structure *Fm3m* where eight oxygen atoms are bound to a metal Ce^{4+} ion. At higher concentrations (x=0.4) only an increase of the full width at half maximum FWHM is observed.

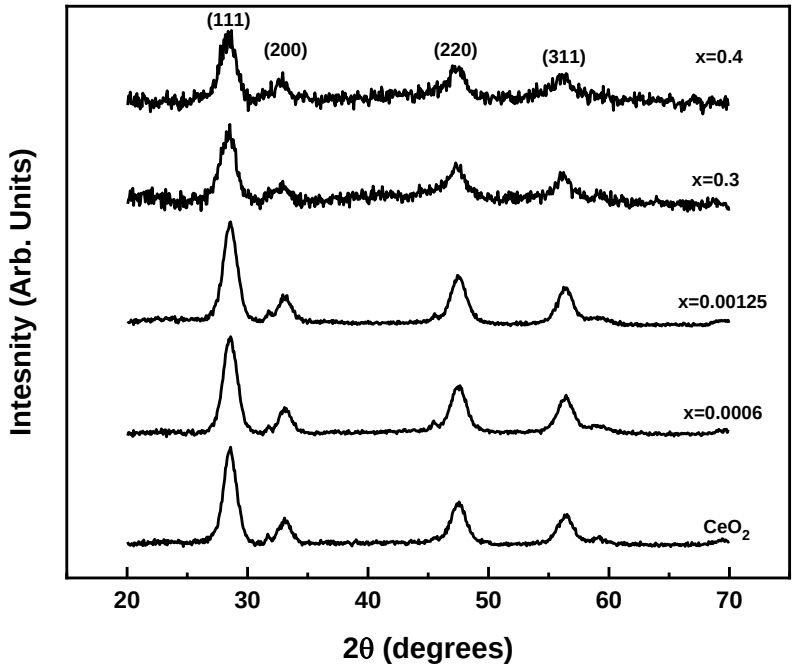

Figure 4.1. XRD patterns of CeO_2:Gd samples deposited onto glass substrates.

From the center of the (111) diffraction peaks the lattice parameters were determined, which we shall discuss in detail later. Complementary information about the cubic phase can be obtained from the Raman spectra of CeO_2, where a triple degeneracy of the F_{2g} mode around 460 cm^1 is evidence of this eightfold oxygen coordination as seen in Figure 4.2. Raman in-situ measurements as a function of temperature were carried out to reproduce the annealing treatment. We can observe how around 250 °C the F_{2g} mode starts to appear, indicating a change between amorphous and polycrystalline phases, below this temperature the contribution around 550 °C and 700 °C due oxygen vacancies (OV) in the

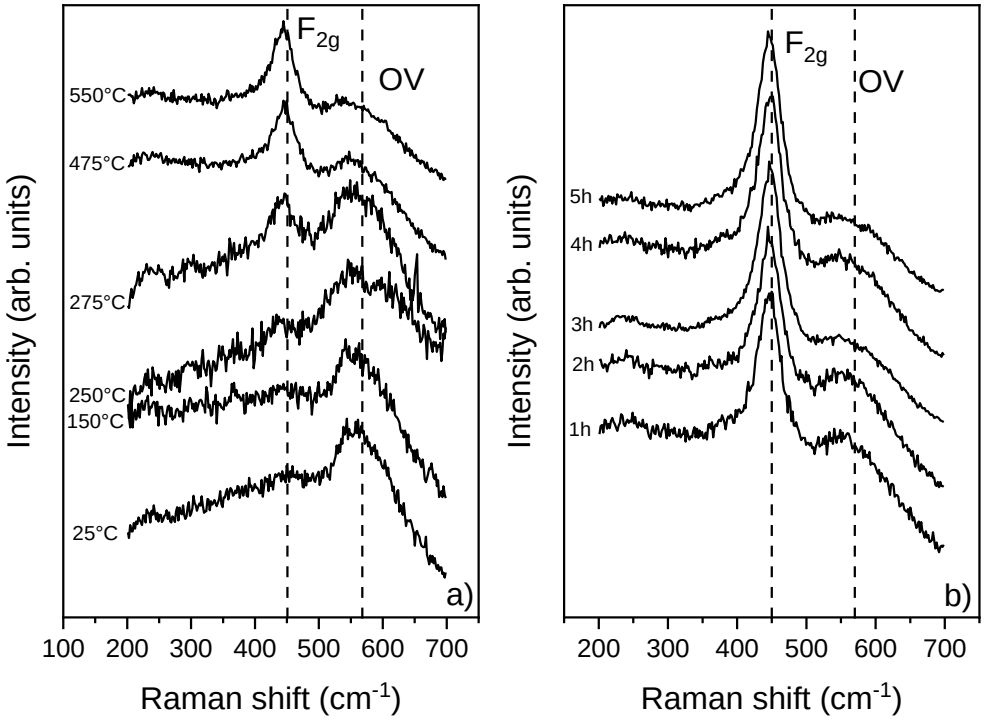

Figure 4.2. F_{2g} mode a) as increasing temperature from 25 to 550°C b) after five hours of treatment

lattice is observable, this is evidence that up to this point, some reduction process Ce^{4+} to Ce^{3+} have taken place, Ce-O bonds coexist in amorphous phase and with the annealing procedure the crystallization process leads to the formation of 8O-Ce structures with OV around.

Strain in the CeO_2 lattice.

The lattice parameter obtained from XRD curves has a specific behavior which is shown in Figure 4.3, the $Ce_{1-x}Gd_xO_{2-x/2}$ system for small concentrations $x < 0.005$ has negligible variations and the lattice parameter remains at 0.5407 nm, while for $x>0.1$ an expansion is observed like that reported for other authors showing the crystallization and substitution of Ce by Gd into the lattice.

It has been mentioned in previous works [32], that the behavior of the lattice parameter doesn't follow the Vegard's rule, and this is because for every two Gd^{3+} incorporated in the lattice, an oxygen vacancy is created.

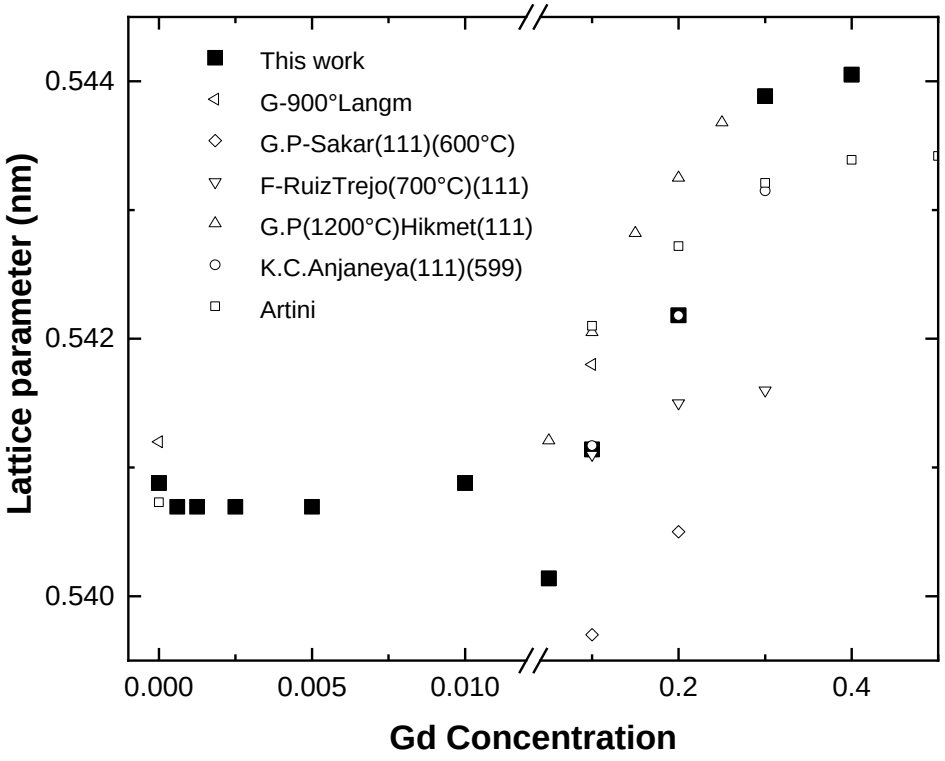

Figure 4.3. Lattice parameter as a function of Gd concentration.

This curvature is then the compensation of two components:

- A force caused by bond stretching i.e. a change in the bond distance due to the replacement of Ce^{4+} by Gd^{3+}
- A strain produced by the generation of oxygen vacancies and in specific cases the strain produced by the substrate.

Notice that this parabolic curvature is shown either if the samples are powders or films, they have different annealing and sintering temperatures and are independent of the synthesis method. Our samples have similar lattice parameters that are comparable with the results from Artini et al. even when they use temperatures of 1200 °C for the thermal treatment. Then we can interpret Figure 4.3 that these changes in lattice parameters may be originated by different strain components due to dissimilar oxygen vacancies density produced by the particular experimental conditions in each report.

From this point of view, Raman spectrum contains information about the compensation of these two components in terms of the shift produced in the before mentioned main phonon for the crystalline structure in CeO_2, the F_{2g} mode.

Figure 4.4 a). shows the Raman spectra for different concentrations of Gadolinium. The spectrum of cerium oxide has two characteristic main phonons, one close to 460 cm^{-1} (F_{2g}) corresponding to the fluorite structure and a weak contribution from 500 to 600 cm^{-1} assigned to oxygen vacancies (OV). Different features of the Raman spectra give information about the incorporation of Gd in the lattice, the first is an intensity increment of the OV phonons, since as the Gd concentration increases in the lattice more vacancies are formed, the second is a shift (blue or red shift) and broadening (in some works called a hump) of the F_{2g} phonon, and the third is the a contribution from 190 cm^{-1} to 370 cm^{-1} attributed to the modes A_g + F_g and (OV). At high Gd concentrations (x > 0.3), these three factors have been reported and correlated to the generation of Gd_2O_3 nanodomains [25]. On the other hand, at low Gd concentrations (x < 0.05), the F_{2g} phonon wavenumber decreases compared to that of CeO_2.

These variations in the spectra can be explained by the spatial correlation model, which accounts for the shift and broadening of a phonon lineshape induced by impurities or defects, using the phonon correlation length (L) as a fitting parameter [28,29]. This length should be infinity in a perfect crystal and is usually < 10 nm in doped semiconductors. In the low Gd concentration interval, L = 6 nm for CeO_2 and it reduces to around 1.5 nm for x = 0.0006, 0.00125, 0.0025 and 0.005, increasing to an average of 2.5 nm for x > 0.01. Thus, the phonon shift is produced by Gd doping at low concentrations, but this effect becomes negligible as Gd concentration increases and the shifts induced by bonding and strain become dominant. The XRD and Raman results are consistent with a behavior of the material as Gd doped CeO_2 (CeO_2:Gd) for x < 0.05 and as a compound ($Ce_{1-x}Gd_xO_{2-x/2}$) for x > 0.05.

In a semiconductor compound, the shift of its main phonon, is given by $\Delta\omega = \Delta\omega_{bond} + \Delta\omega_{strain}$, where $\Delta\omega_{bond}$ is produced by the bond stretching due to the substitution of

Gd^{3+} by Ce^{4+} in the lattice, as a result of bond length variation. The variation $\Delta\omega_{strain}$ originates by the contribution of the substrate and oxygen vacancies. On the other hand, the shift $\Delta\omega_{bond}$ is proportional to the change Δa in the lattice parameter, and it can be written as $\Delta\omega_{bond} = -3\gamma\omega_0\Delta a / a_0$ [10]. Here, ω_0 is the Raman wavenumber of CeO_2, a_0 is the CeO_2 lattice constant, and γ is the Grüneisen parameter which depends on the CeO_2 bulk modulus and on the shift of Raman frequencies with hydrostatic pressure. We used the parameter value obtained by Sato and Tateyama of γ = 1.24 [33]. With a linear fit of $\Delta\omega$ in the concentration interval x > 0.1 and following Ref 10 we obtain: $\Delta\omega$ = -16.34x cm^{-1}, $\Delta\omega_{bond} =$ 28.66x cm^{-1} and $\Delta\omega_{strain} =$ -45x cm^{-1}. The contributions of opposite sign to the total phonon shift are shown in Figure 4 b) dotted lines for clarity. If the oxygen vacancy density could be controlled and quantified, which is out of the scope of this work, Raman spectroscopy could be used as a tool to estimate the vacancy density in this compound.

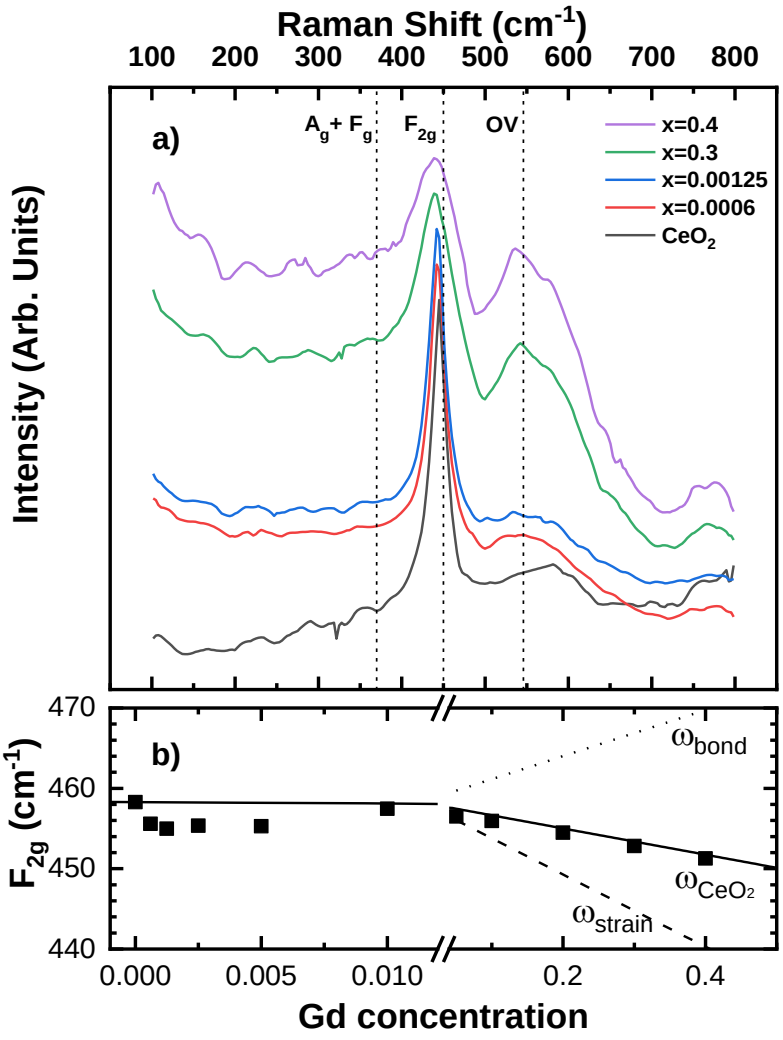

Figure 4.4. (a) Room temperature Raman spectra of $Ce_{1-x}Gd_xO_{2-x/2}$. The spectra are vertically displaced for clarity with increasing Gd concentration from bottom to top. (b) Raman shifts of the F_{2g} phonon as a function of Gd concentration. The dotted lines with slopes of 28.66 and -45 cm^{-1} indicate the contributions of atomic bonding and strain respectively, for a net shift of -16.34x cm^{-1} , given as a solid line.

Strain of CeO_2 films on silicon (001) substrates.

For films deposited on silicon, the $Ce_{1-x}Gd_xO_{2-x/2}$ system has a different behavior, in Figure 4.5 we can observe again the F_{2g} phonon as was observed on glass samples but now the phonon is accompanied with a signal around 430 cm^{-1} (marked by an arrow on Figure 4.5) not observed on glass samples, and the phonon for concentrations x>0.2 has three Lorentzian perfectly separated in contrast with the previous ones where only a broad phonon was appreciated

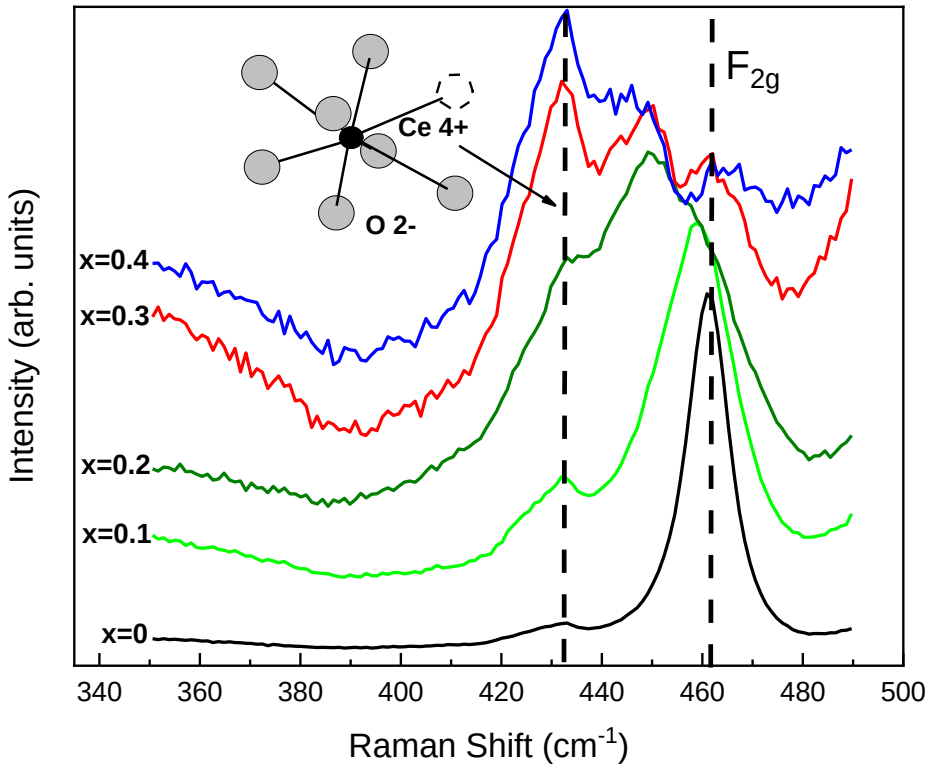

Figure 4.5 Room temperature Raman spectra of $Ce_{1-x}Gd_xO_{2-x/2}$ for different gadolinium concentrations on Si(001) substrates. (it would be helpful to plot these spectra as in figure 4.4 from 100 to 800 cm-1, or what happens with OV in this case???)

By changing the substrate is supposed that the strain component has a different contribution, and this effect could be corroborated if we do the same analysis for the F_{2g} mode for these samples. Figure 4.6 has a comparison of the F_{2g} shift as function of the Gd concentration for samples on glass and silicon substrates.

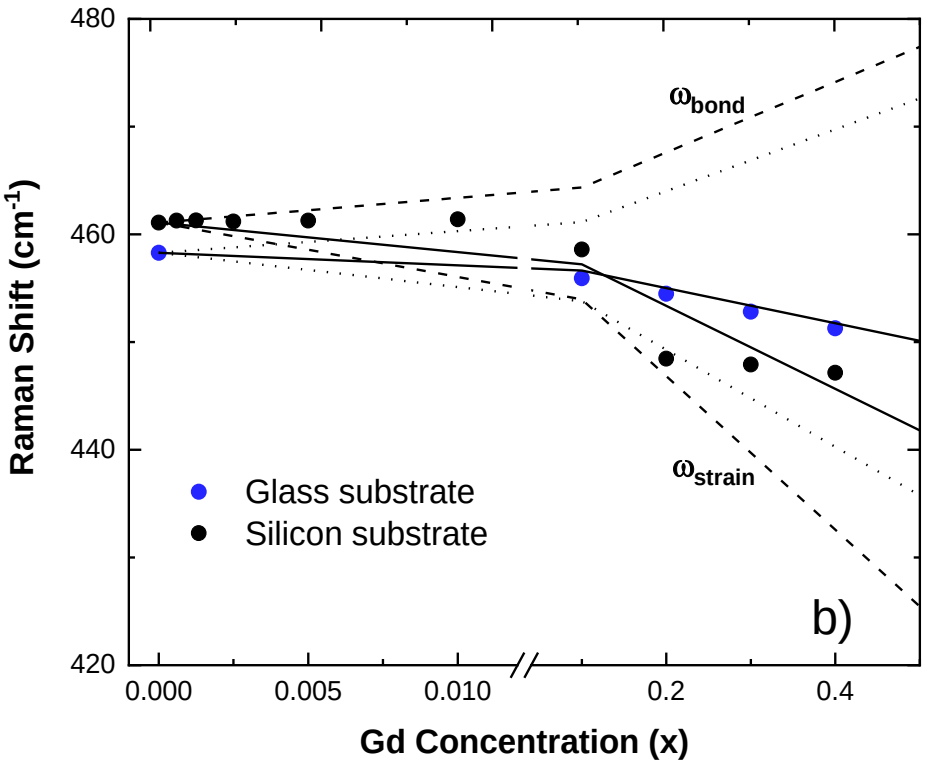

Figure 4.6. Raman shifts of the F_{2g} phonon as a function of Gd concentration for different substrates. The dotted lines with slopes of 28.66 cm^{-1} and -45 cm^{-1} indicate the contributions of atomic bonding and strain respectively on glass, and in dashed lines.

In black circles and dashed lines the $\Delta\omega_{strain}$ and $\Delta\omega_{bond}$ components for the samples on Si(001) are shown, the values obtained were -71.23x and 32.67x respectively, if we compare these results with the obtained on glass substrates Table 1. We could notice that the strain component $\Delta\omega_{strain}$ is changing by -26.23x while the $\Delta\omega_{bond}$ component just by -4.01x this corroborates the influence of the substrates and as well a change in the substrate may modify the OV generation in a different way explaining why we can observe the phonon around 430 cm^{-1}.

Table IV.I. Total shift components for $Ce_{1-x}Gd_xO_{2-x/2}$ samples on glass and silicon substrates.

Substrate	$\Delta\omega_{strain}$ (cm^{-1})	$\Delta\omega_{bond}$ (cm^{-1})	$\Delta\omega$
Glass	-45x	28.66x	-16.34x cm^{-1}
Silicon (001)	-71.23x	32.67x	-38.56x cm^{-1}

Rupture of symmetry of F_{2g} mode.

In the literature the common Raman modes are around 500 cm^{-1} and 600 cm^{-1} which always come aside of the F_{2g} mode, and are called OV phonons, nevertheless a vacancy is a space on the lattice which only helps to keep the charge due to the contribution of Ce^{3+} then it is not possible that a space in the lattice vibrates around an equilibrium position. What occurs is that the F_{2g} mode suffers a rupture of symmetry i.e the Ce^{4+} suffers a different strength by changing the eightfold O coordination surrounded and the modes observed up and below this main phonon came from different interactions with more and less oxygen atoms. The way to obtain an interaction of oxygens either with Ce^{4+} or Ce^{+3} have been done using greens functions [34] where they proposed different configuration for a metal and a space in the lattice. In a simple way to understand the mode around 430 cm^{-1} we have used a simple Raman used before for SiGe [35]. We shall consider that oxygen atoms are moving, and the Ce atom remains static ($m_O/m_{Ce} \rightarrow 0$), the F_{2g} mode is produced by an eightfold O around Ce, in this case ω_0 must be given by:

$$\omega_0^2 = \left(\frac{1}{m_{Ce}}\right)\sum_{i=1}^{8} k_i = (k_0/3m_{Ce})(1+1+1+1+1+1+1+1) \quad (4.1)$$

With an oxygen vacancy in the lattice, Figure 4.7, we have:

$$\omega^2 = (k_0/3m_{Ce})(1+1+1+1+1+1+1) \quad (4.2)$$

Where:

$\omega/\omega_0=\sqrt{7/8}$= 0.93

The wave number for F_{2g} mode ≈ 460 cm^{-1} will be affected by this factor, throwing 427.8 cm^{-1}, this corresponds to the mode at 430 cm^{-1}, dashed line in Figure 1 a), notice how this mode intensity increases as more oxygen vacancies appear when Gd atoms are added into the lattice

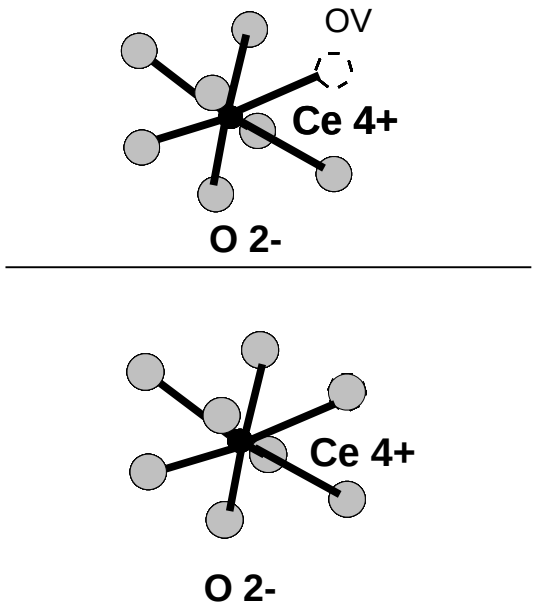

Figure 4.7. Diagram for F_{2g} rupture of symmetry assuming that ($m_O/m_{Ce} \rightarrow 0$).

X-Ray photoelectron spectroscopy (XPS).

The samples were analyzed by X-ray photoelectron spectroscopy (XRD) where the stoichiometry can be analyzed as increasing the Gd concentration. For the whole range XPS shows the *O1s* characteristic peak, the characteristic *Ce 3d* and *Gd 3d* core levels as well as *Ce 4s, 4p, 4d, 5p* and *Gd 4p, 4d* are observed (Figure 4.8.)

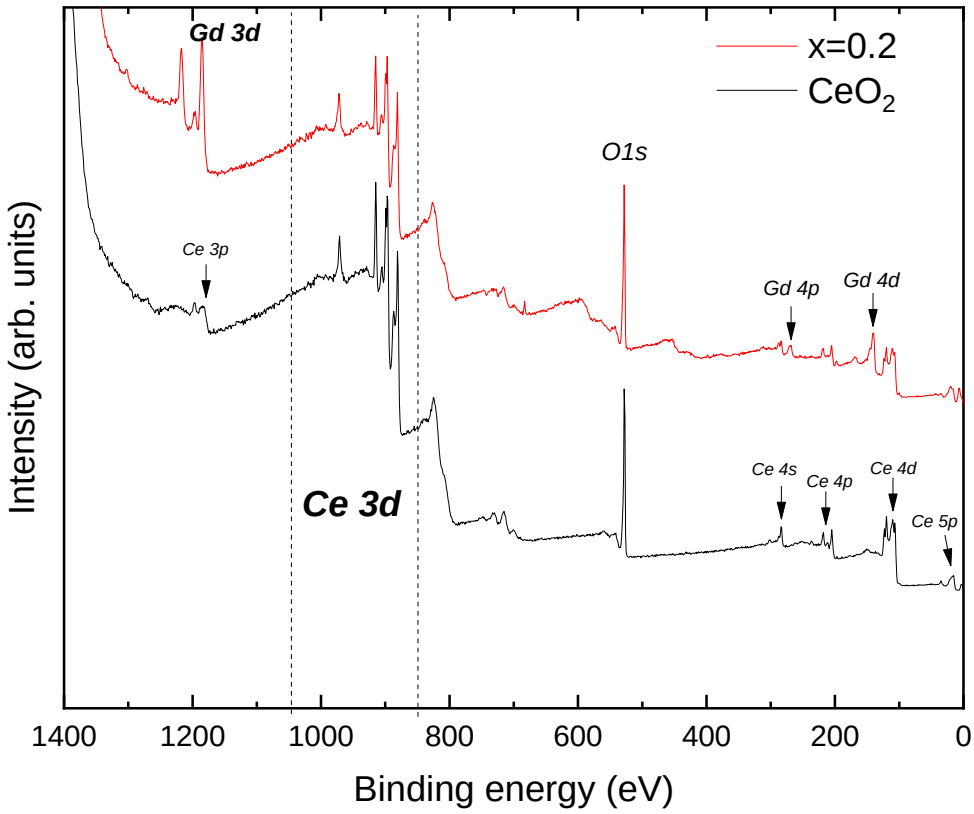

Figure 4.8. X-Ray photoelectron spectroscopy measurements for CeO_2 and CeO_2:Gd with x=0.2 for samples dried at 90 °C.

To determine the amount of Gd and Ce in the lattice the *Ce 3d* and *Gd 3d3* (was used because of the coupling between *Ce3p* and *Gd 3d5)* peak intensities were compared with O1s to know the amount of Ce^{4+} and Gd^{3+} the results are shown in Table lV.2.

Table lV.II. Percentage of Ce and Gd from the ratio of intensities by XPS

Gd concentration x	$[O]_{1s}$ (%)	$[O]_{1s}/[Ce]_{3d}$ (%)	$[O]_{1s}/[Gd]_{3d3}$ (%)
x=0	-	-	-
x=0.1	74.98	15.69	9.34
x=0.2	74.98	15.69	9.34
x=0.3	75.22	12.38	12.38
x=0.4	74.5	12.27	13.23

It is possible that Ce forms two different structures CeO_2 and Ce_2O_3 and with the Gd incorporation is possible as well Gd_2O_3, nevertheless XRD doesn't show peaks contributions of this phases and from the Raman spectra we know that Ce^{3+} is consumed in oxygen vacancies.

One way to identify the amount of Ce^{3+} that we have in the lattice is from the *Ce 3d* core level. Burroughs et al. have labeled the contribution of the peaks of this level as follows [36]

For Ce^{4+} U''' and V''' result from the Ce3d^9 O2p^6 Ce4f^0 final states. The additional U, V, U'', V'' result from a mixture of Ce3d^9 O2p^5 Ce4f^1 and Ce3d^9 O2p^4 Ce4f^2 and the contribution of the Ce^{3+} to the spectra consist of two doublet pairs U' V' and U_0 V_0 and they came from a mixture of Ce3d^9 O2p^5 Ce4f^2 and Ce3d^9 O2p^6 Ce4f^1final states [37]. To determine the amount of Ce^{3+} we used the $[\mathrm{Ce(lll)}] = \mathrm{Ce(lll)}/(\mathrm{Ce(lll)} + \mathrm{Ce(lV)})$ [Feng Zhang Cerium oxidation state] where $\mathrm{Ce(lll)}$= V_0 + V' + U_0 + U' and $\mathrm{Ce(lV)}$= V+ V'' + V''' + U + U''+ U''' are the sums of the integrated peaks area shown in Figure 4.10.

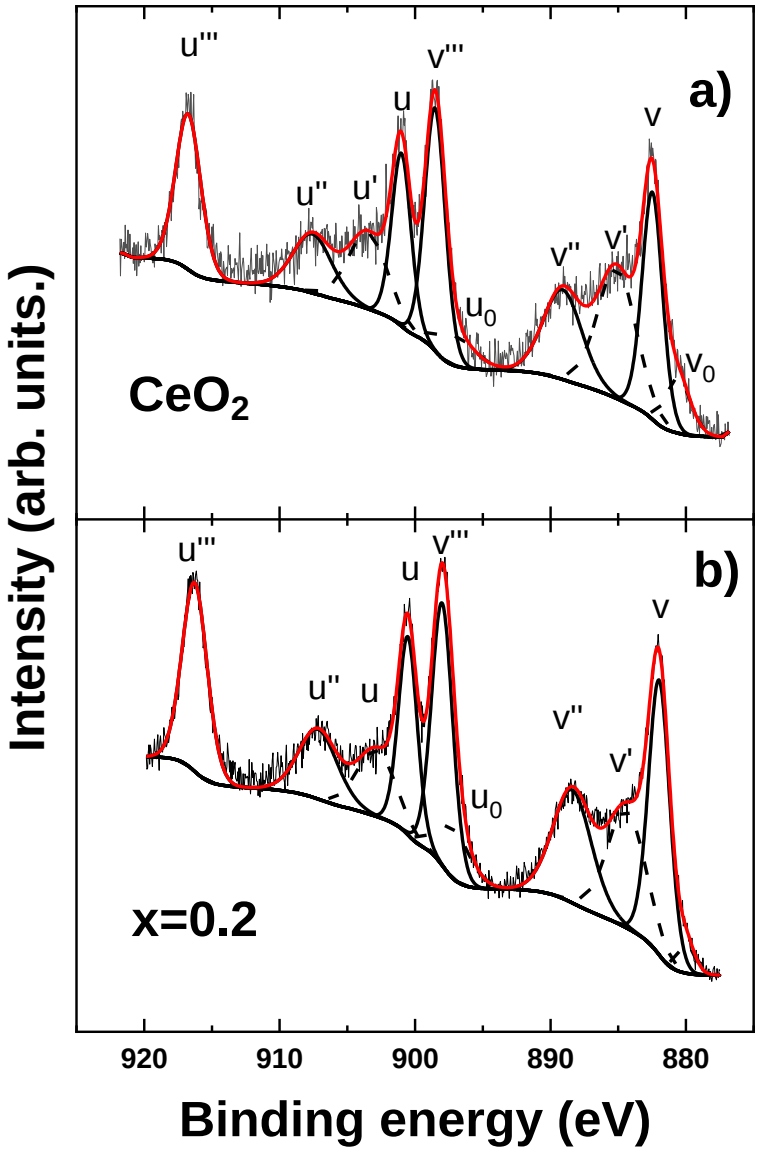

Figure 4.9 XPS for 3d level a) in CeO_2 b)with a Gd concentration of 0.2, in in solid lines the contribution by Ce^{4+} in dashed lines which came from Ce^{3+}

The percentage of Ce^{3+} for the different Gd concentrations is displayed in Figure 4.10, it is important to show the amount of Ce (lll) reaches a minimal value for the concentration of x=0.2, decreasing from 31.6 % to 25.5%, considering that for each two trivalent Ce^{3+} ions one vacancy should be generated, with this at least 15.8% should be spaces in the lattice (OV) and the incorporation of Gd near x=0.2 give us 12.75 % a reduction in the OV formation (contrary to the well-known property for these material and also contrary to the Raman results (modes around 500 and 600 cm^{-1})) this phenomenon was first observed by Holger Borchet et al. where they found that increasing the Gd content leads to a decreasing of the Ce^{3+}. And this argument can´t be supported because there is a segregation due to the Ce^{4+} to Ce^{3+} reduction process, observed by the decreasing in Ce-Gd ratios [38], also seen in Table l. Then the Ce^{3+} percentage could be underestimated.

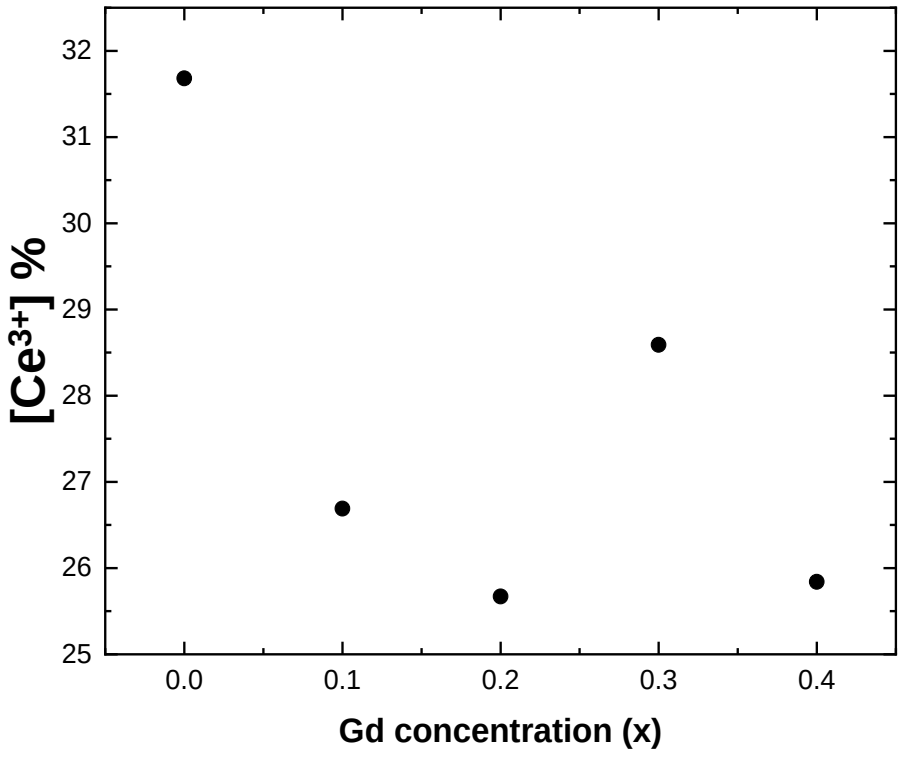

Figure 4.10. Percentage of Ce^{3+} in the lattice as a function of the Gd concentration.

The Gd *3d* is observed in Figure 4.11, the main feature is that a and b-contributions are affected as we increase the Gd concentration, another aspect here is that the a/b spin-orbit splitting is composed by three Gauss-Lorentzian peaks in contrast with [39] where they are completely separated

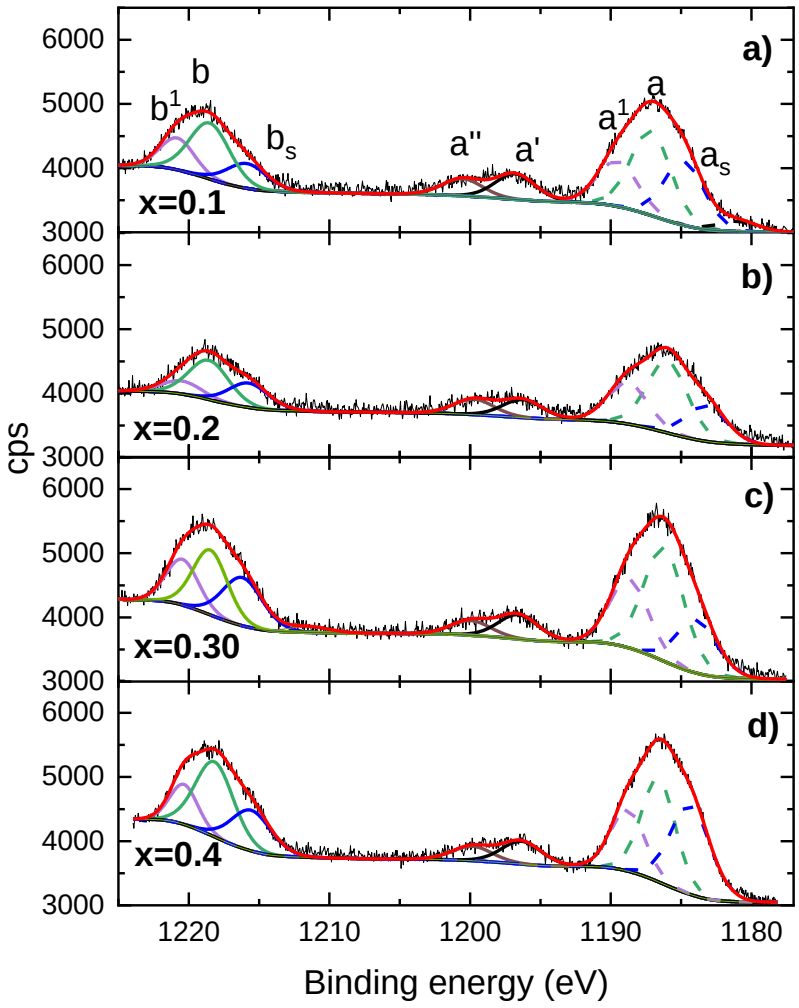

Figure 4.11 Gd 3d level as a function of the Gd concentration.

The centers of the peaks are summarized in Table lV.lll. in our case the main doublet a/b has the peak $3_{5/2}$ centered in 1187.14 eV with a spin-orbit splitting of 33.73 eV , the satellite features lies around 1196.79 eV and 1200.55 eV, for the b' and b'' difference arise in our results because a_s and b_s have a different contribution in our spectra centered at

1184.78 eV and 1215.85 eV respectively while a^1 and b^1 have 1189.52 eV and 1220.82 eV.

Table lV.lll. Peak centers for the Gd *3d* level

Gd concentration (x)	a_s (eV)	A (eV)	a^1 (eV)	a´ (eV)	a´´ (eV)	b_s (eV)	b (eV)	b^1 (eV)
0	-	-	-	-	-	-	-	-
0.1	1184.78	1187.14	1189.52	1196.79	1200.55	1215.85	1218.51	1220.82
0.2	1183.2	1185.97	1188.78	1196.27	1199.73	1215.73	1218.57	1220.49
0.3	1183.89	1186.22	1188.68	1196.57	1199.95	1216.18	1218.47	1220.46
0.4	1184.34	1186.61	1188.77	1196.34	1199.84	1215.56	1218.17	1220.34

F-Centers in CeO_2:Gd

In samples of CeO_2:Gd on glass substrates, it was found the formation of well-defined crystals, such as those shown in Figure 4.12.These crystals have a specific concentration of Gd, as shown by the behavior of the F_{2g} mode Figure 4.12 c), also was found by micro-photoluminescence emission by defects called *F-centers*, which were already discussed in the introduction, only emphasizing that as the concentration of Gd in each crystal increases the same emissions reported in [14] Figure 4.12 b) are observed. As the crystal size decreases, i.e. in films around 255nm a simple splitting (inset graph in Figure 4.13), and when measuring in thicknesses close to 100 nm, this splitting disappears. It is possible

to appreciate in Figure 4.12 e) that each crystal grows with the specific concentration of Gd which is corroborated by the phonon symmetry breaking, and in Figure 4.12 d) marked with arrows we can see the emissions by F-centers promoted by gadolinium.

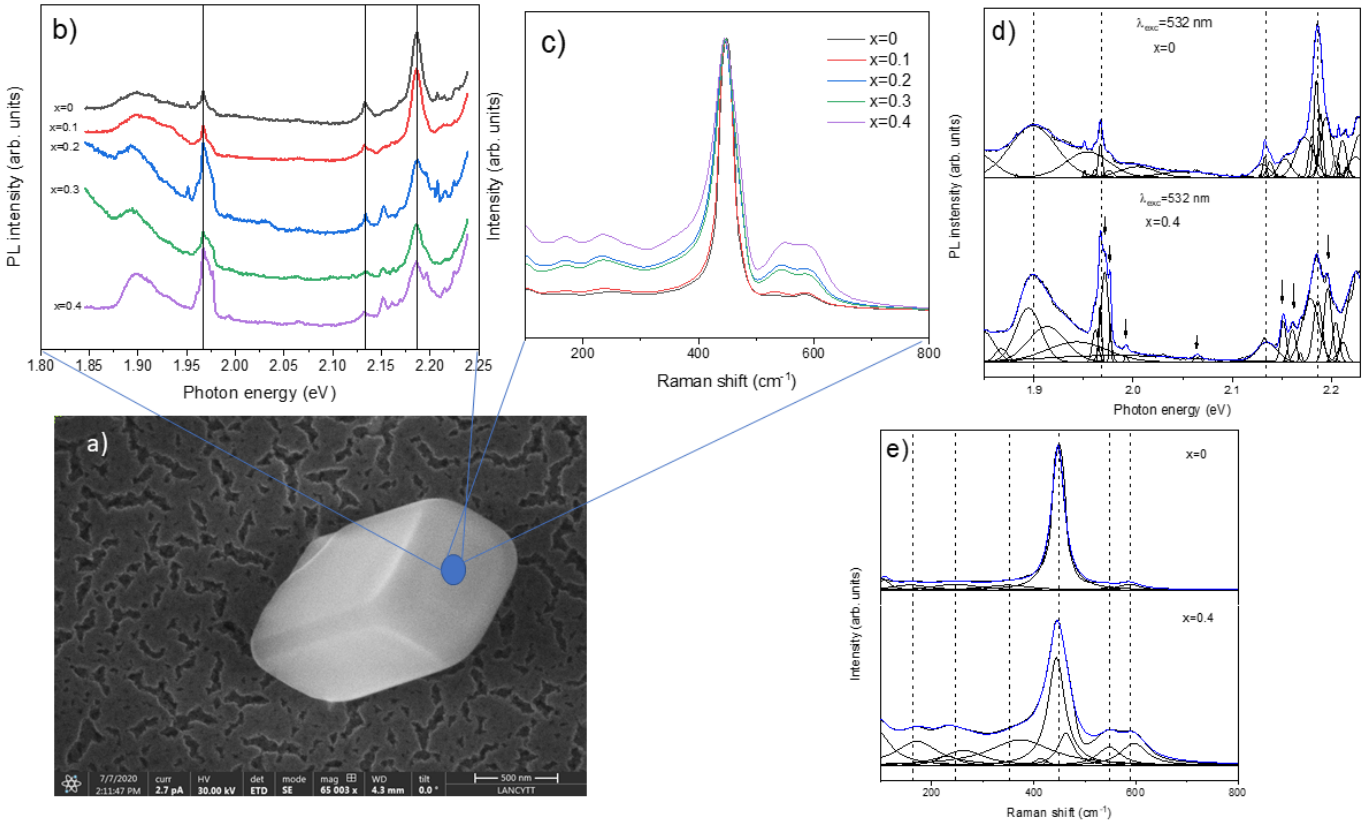

Figure 4.12. a) Micro-Photoluminescence spectra from crystal with x=0, b) Micro-Photoluminescence spectra from crystal with x=0.4 using an excitation source of λ_{exc} = 532 nm at room temperature.

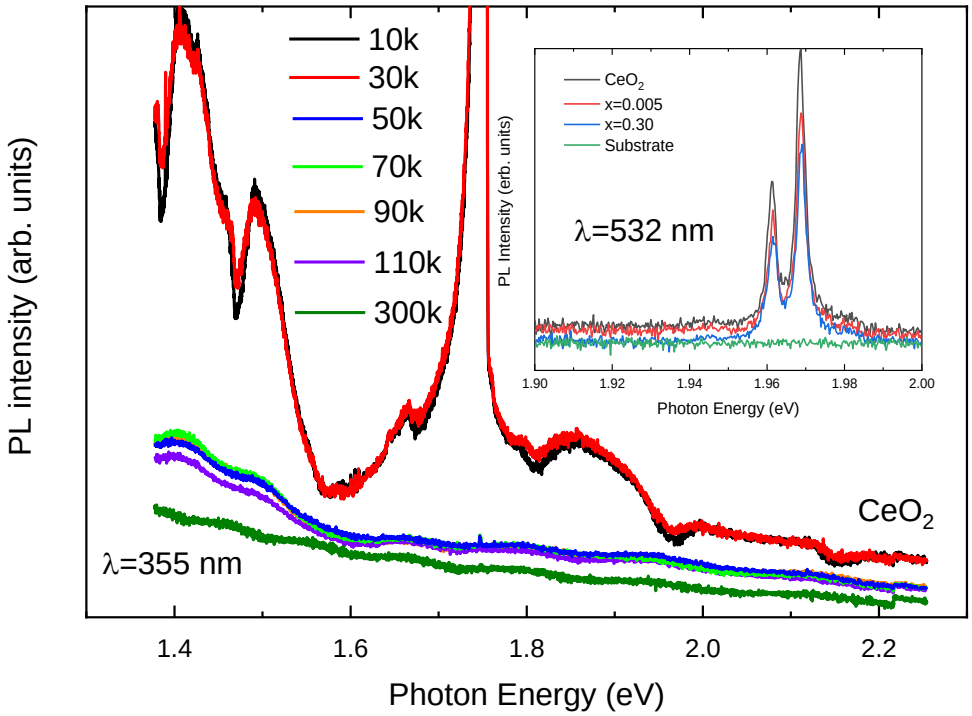

Figure 4.13. PL spectra of CeO_2 sample, in inset micro-PL for samples of 250 nm of thickness with different Gd concentration.

Dielectric function of CeO_2:Gd/Si(001).

Regardless the dielectric function of the material, the section was distributed as follows:

i) The analysis of the samples dried at 90 °C on Si(001) with a Woollam ellipsometer in the range from 0.734 to 6.477 eV for two concentrations x=0, and x=0.3 where two models where used a double Tauc-Lorentz and a B-Splain to compare the dielectric function of the material at different Gd concentrations.

ii) The analysis of the samples dried at 270 °C with a Horiba-Uvisel ellipsometer in the range of 0.6 to 4.75 eV

Dielectric function of samples dried at 90°C on Si(001)

In Figure 4.14 the Fourier coefficients pseudo dielectric function is shown for a CeO_2:Gd, in dots the fit from a B-Spline model, the thickness of the films lies between 71.69 nm and 98.2 nm and parameters are compared listed in Table lV.lV to compare the consistency with the doble Tauc-Lorentz model.

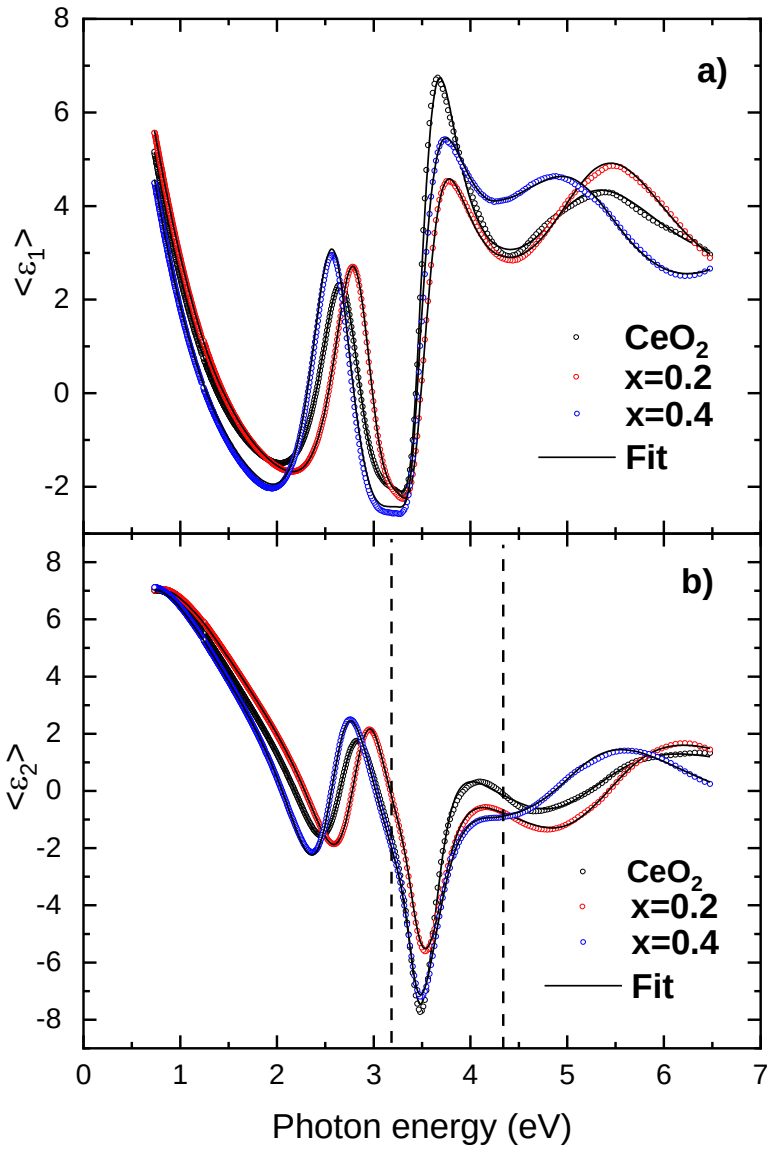

Figure 4.14. Pseudo dielectric function for different Gd concentrations using a B Spline model.

Table lV.lV Parameters from both B Spline and double Tauc-Lorentz.

Gd concentration (x)	*B-Spline*			*thickness (nm)*	*2Tauc-Lorentz*				*thickness (nm)*
	ε_∞	n	k		E_{g1}	E_{01}	E_{g2}	E_{02}	
0	1.203	1.5	0	75.45	2.14	5.48	2.917	3.932	78.27
x=0.3	1.99	1.5	0	98.12	1.797	5.217	2.886	3.974	101.51

Dielectric function of samples dried at 270°C on Si(001)

A double Tauc-Lorentz model was used to fit the Fourier coefficients Is and Ic Figure 4.15 a) we used this model for all the Gd concentrations, the thickness for these films were around 250 nm. The model shows the transition which corresponds to O2p - Ce4f around 3.2 eV, as we can see in Figure 4.15 b) for the ε_1 and ε_2 extracted from the first Tauc-Lorentz (TL1) (Dark filled and open circles), in Figure 4.15 c) we have the substrate contribution.

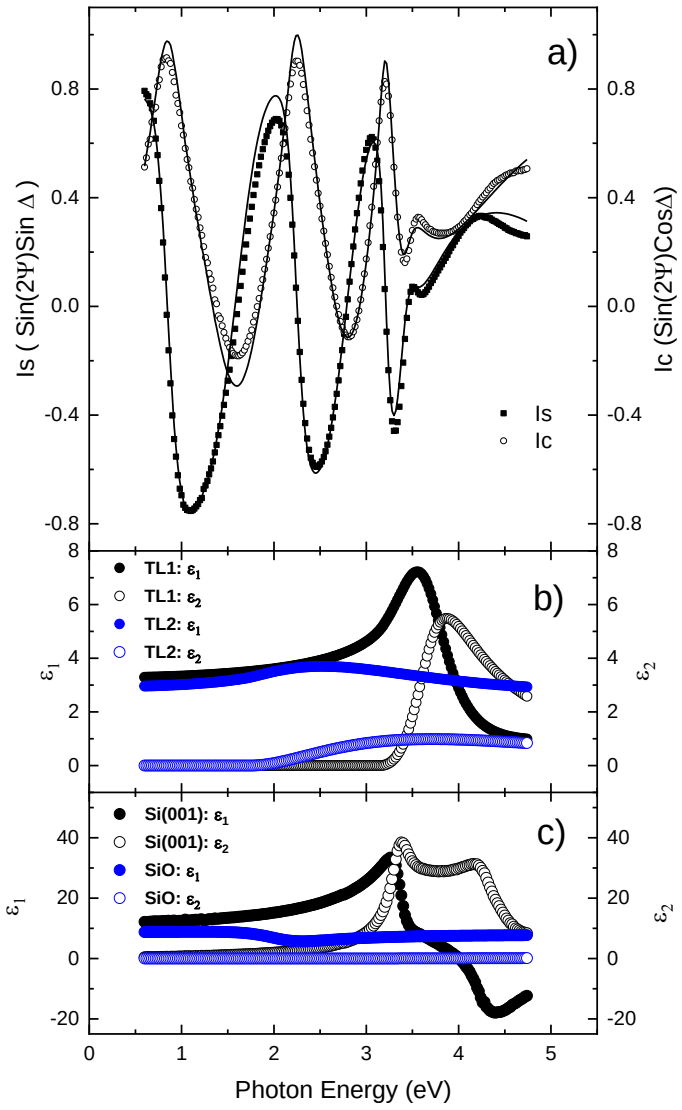

Figure 4.15. Ellipsometry model for CeO_2 sample a) Fourier coefficients Is and Ic in solid lines the Fit using a double oscillator Tauc Lorentz model b) real ε_1 and imaginary ε_2 part of the dielectric function.

Anisotropies on CeO_2 :Gd.

Knowing that for concentrations 0.1 ≤ x ≤ 0.3 the material has an unusual behavior of its properties and by means of the proposed model above we observed that strain and bonding contributions can be separated, the samples were analyzed by RAS.

To understand the nature of the RAS signal, measurements with different Gd concentrations were made for different in-plane angles: 0°, 45° and 90° with an increment of 10°. Figure 4.16 shows the real (Ic) and imaginary (Is) part of the RAS signals for x=0 , x=0.3 and for a (001) Si substrate. The variations of the signal in the 2.2 eV to 4.3 eV range (region between dashed lines) is more evident in the sample with x = 0.3 and for 55° and 85° the imaginary part of the signal flips completely (remarked with arrows in Figure 4.16 d)) producing that the real part of the signal reaches positive values.

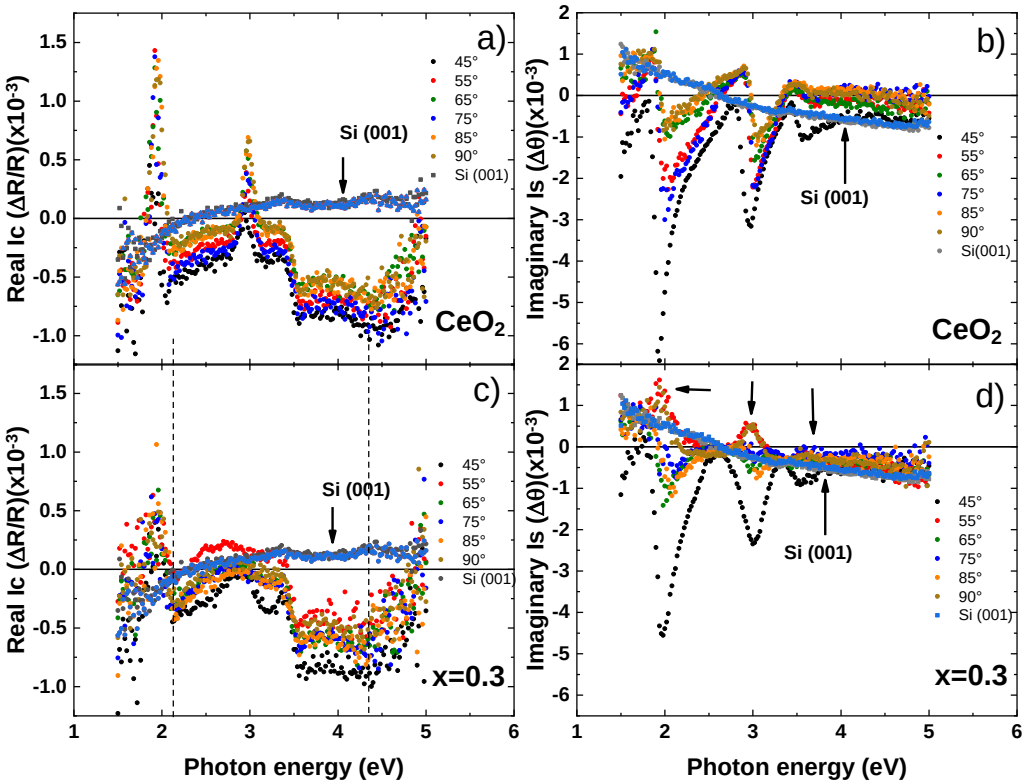

Figure 4.16. Real (Ic) and imaginary (Is) part of RAS signal for different in-plane angles a) and b) for a concentration of x=0 c) and d) are for x=0.3, the flip of the signal is marked

with arrows and the Si (001) substrate is displayed as a reference in a different angle variation.

Anisotropies can be influenced by the following factors.

- Hexagonal phase clusters from gadolinium substitution.
- Strain induced by Si(001) substrate.
- By magneto-optic effect.

The first is supported by the XPS results where spin-orbital couplings are observed near 1200 eV indicating that the strain potentials are acting on the film and that both the gadolinium substitution and the percentage obtained lie within the desired range of concentrations.

For the second one we use a model proposed in [24], using equation (2.8) to fit the RAS signal obtaining Figure 4.17. A comparison of different angle signals was done by subtracting the spectra of maximum observed variation. Additionally, we used the specific dielectric function of each concentration to get the complex reflectivity and plot the real part of ($\Delta R/R$) following equations 2.3 and 2.4. Figure 4.17 shows the fit using equation 2.8 with values A=1.5 x10^{-4} and B=3 x10^{-4}, for x=0. We can observe how the signal around 3 eV is less intense when the lineshape comes from 65°-75° than the one from 45°-90°, nevertheless signals above 3.2 eV are not observed for x =0. On the other hand, for x=0.3 a signal near 3.5 eV survives to the subtracting process in Figure 4.17 b). Finally in Figure 4.17 c) the signal was plotted with critical values of the constants A and B to separate the lineshape from the substrate and from the film, this aid us to understand why some transitions disappear completely in the range from 3.5 to 4 but they are observed when A=3x10^{-4} and B=0 showing that in this range the signal has a high influence of the *4f* states.

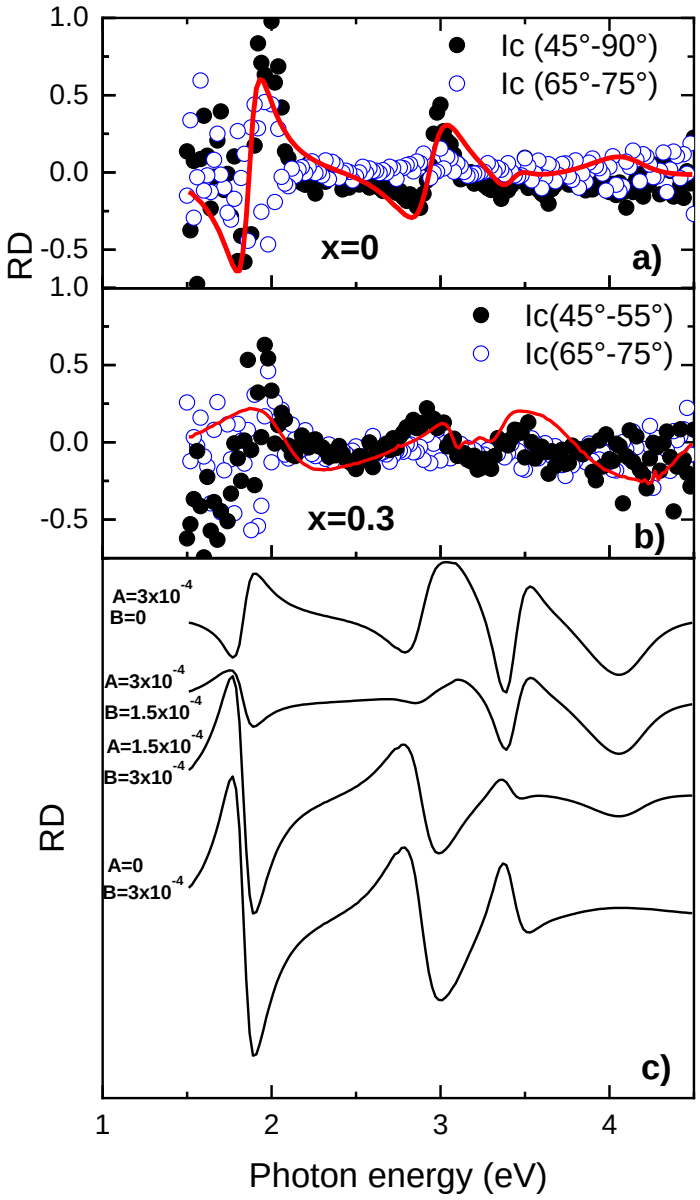

Figure 4.17. RD signal by subtracting critical angles, in solid lines the fit using equation 4 a) for x=0 of the Gd concentration b) for x=0.3 c) the fit of equation 4 for critical values of the constants A and B.

The OA observed for x = 0.3 may be originated by anisotropic strain as the film relaxes with the increment of Gd concentration and oxygen vacancies revealed by Raman spectroscopy. On the other hand, the RAS of strained films with x < 0.1 do not exhibit this behavior.

The third one will be discussed in the next section.

Anisotropies induced by magneto-optic effect.

RAS measurements were obtained on CeO2/Si(001) films with a neodymium magnet ($\mathbf{B} \approx 0.3\mathrm{T}$) (Figure 4.18).

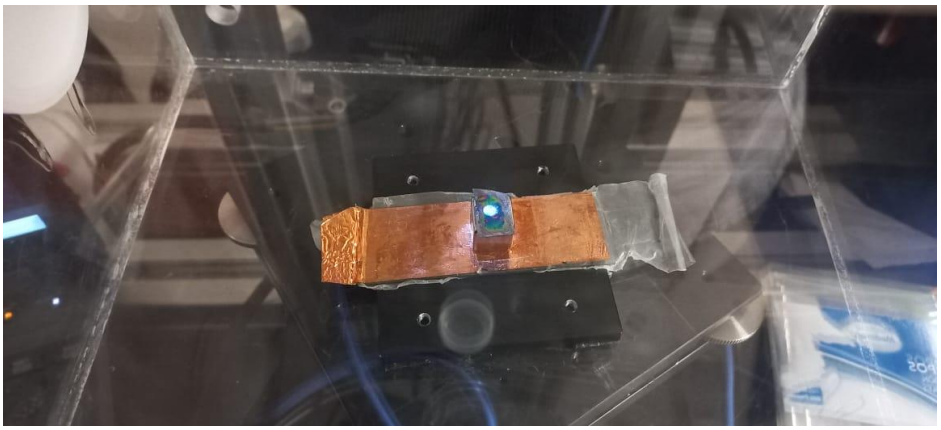

Figure 4.18. RAS configuration with an applied magnetic field using a neodymium magnet.

The line shape when the magnet is inverted and the sample is placed again produces a change in the signal near the 4f level (Figure 4.19), from the dielectric tensor in equation 2.10 and obtaining the Voigt parameter with ellipsometry in presence of a magnetic field it is possible to fit the RAS signal using the program shown in appendix I., The results are displayed in Figure 4.20.

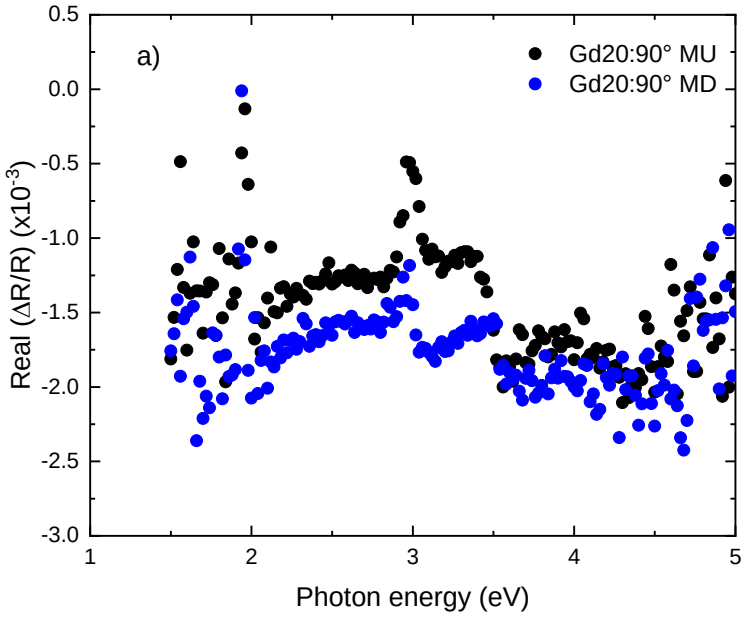

Figure 4.19. Real part of RAS measurement for CeO_2:Gd/Si(001) film with x=0.2 with two magnet orientation (MU and MD).

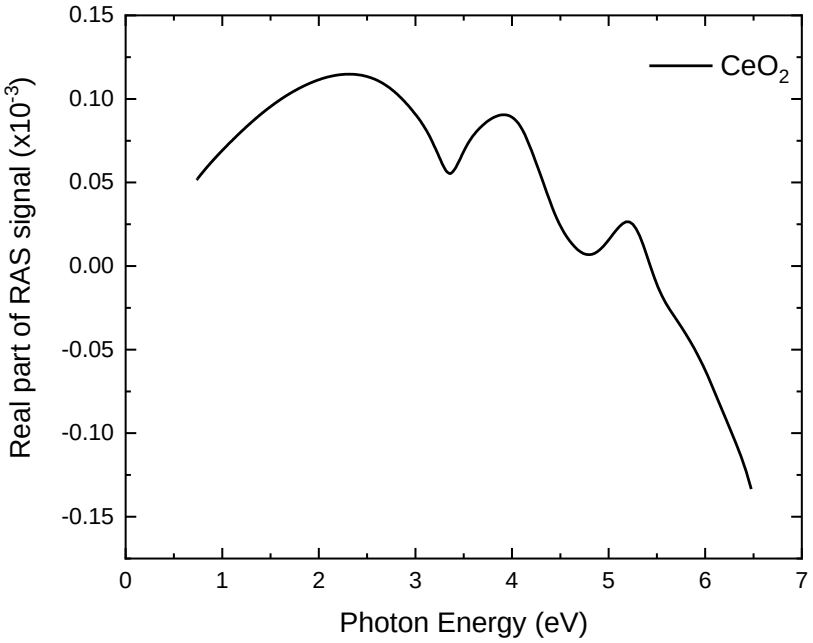

Figure 4.20. RAS Signal for CeO_2 with a Voigt parameter constant of Q =0.336x10^{-4} + i0.0481x10^{4}, using the dielectric function from the SE model.

Given the ferromagnetic nature of the CeO_2:Gd/Si system, the explanation of the decrease in Ce^{3+} concentration as we increase the gadolinium concentration will be as follows:

From XPS a decrease in the percentage of Ce^{3+} is evident, which leads us to think that there must be a decrease in OV, but the Raman results indicate the inverse (since for each two trivalent ions, an OV is generated), a reasonable explanation due to the ferromagnetic nature of Ce^{3+}, Gd^{3+} is that when electrons are ejected from the surface for detection in XPS they tend to be retained by a magnetic field of these ions, by means of the Zeeman effect, so that the Ce3+ concentration is not overestimated as discussed in [28].

Gadolinium doping and photovoltaic applications.

The films at different Gd concentrations were measured by Hall effect, it is possible to see in Figure 4.21 that for concentrations x<0.01 the carrier concentration increases from 10^{14} cm^{-3} a 10^{16} cm^{-3} .

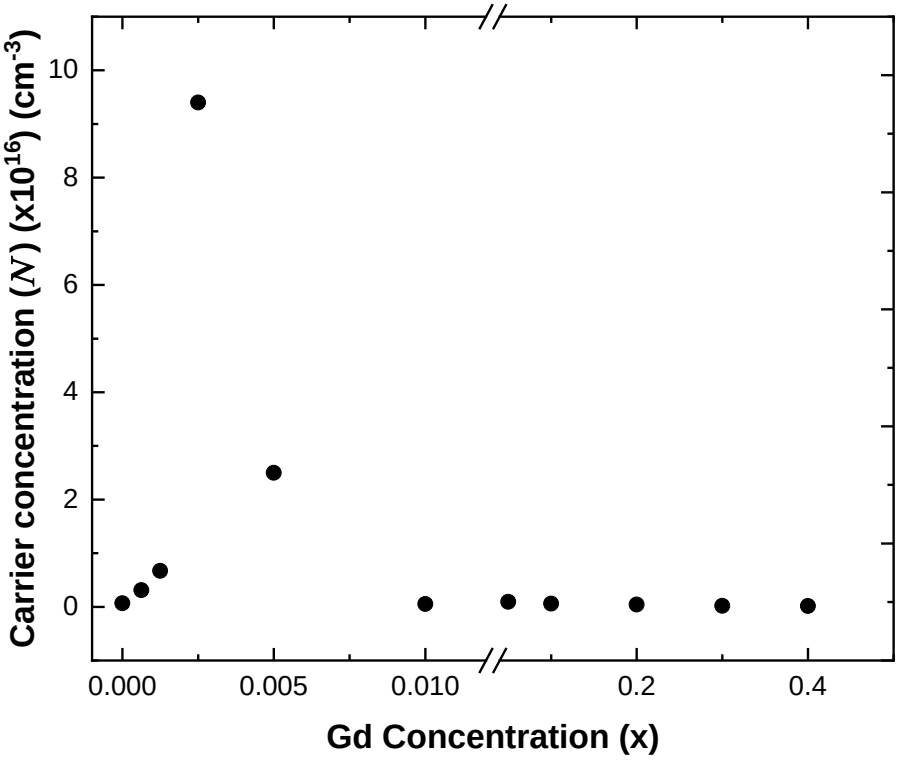

Figure 4.21. Carrier concentration for CeO_2 :Gd films onto glass substrates.

Figure 4.22 shows the p-n junction of the heterostructures of the experimental section Figure 3.2, where it is possible to appreciate the formation of the diode, Figure 4.22 a) shows the activation voltage which corroborates the diode behavior and in Figure 4.22 b) we see the photovoltaic effect with a V_{oc}= 100 mV

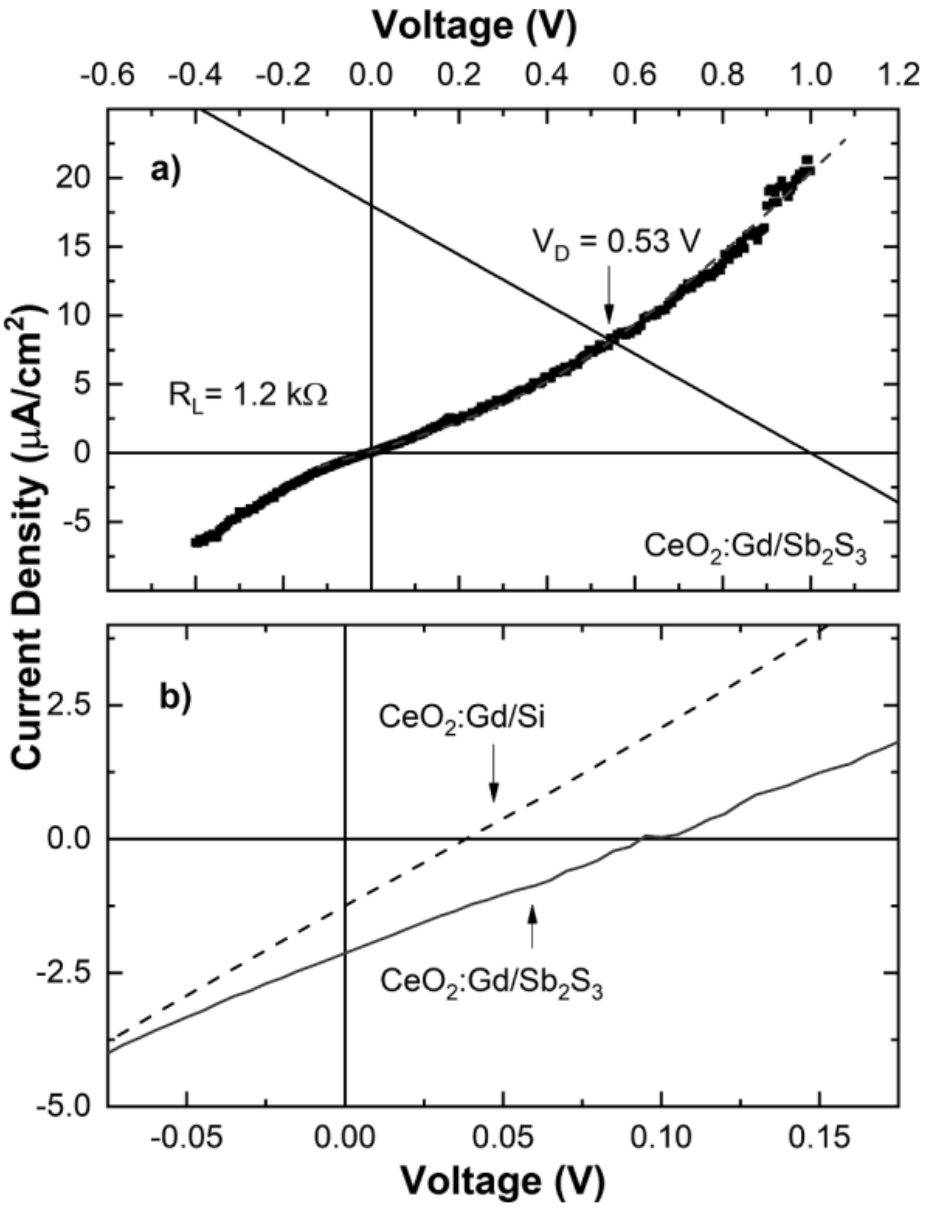

Figure 4.22. (a) Current density vs. voltage curves in darkness of the CeO_2:Gd/Sb_2S_3 junction (solid squares). The load solid line, using a resistance RL = 1.2 kΩ, shows that the forward diode voltage is V_D= 0.53 V. The dashed line is the plot of the implicit diode equation using the parameters obtained from the experimental data. (b) Current density vs. voltage curves under AM1.5 illumination for CeO_2:Gd/Si and CeO_2:Gd/Sb_2S_3 junctions.

In Figure 4.23 we can see how improves the values of the device after a 370°C at room temperature and reaching a V_{oc} = 220mV.

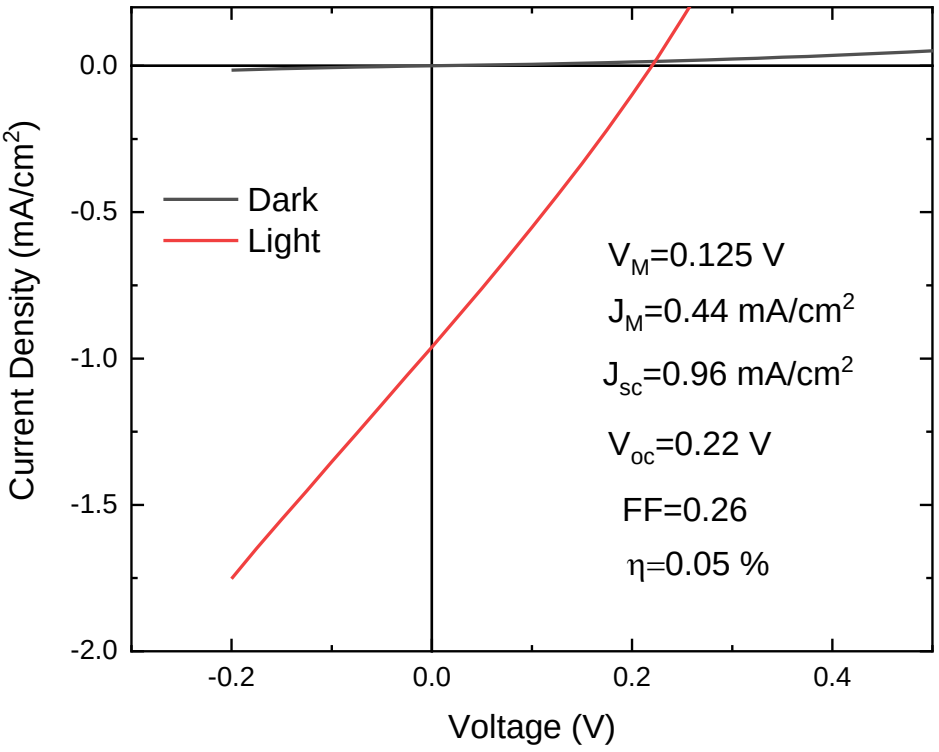

Figure 4.23 Photovoltaic device CeO_2:Gd/ Sb_2S_3 after 370°C heating treatment for 3 min.

Conclusions.

In summary, the optical and electrical properties of the CeO_2:Gd system on Si(001) and glass substrates were studied. Using a Raman model supported by the modification of the dispersion relations, it was possible to separate the strain and substitutional components, where the strain potentials are acting with increasing gadolinium concentration.

Since we have an isotropic material for concentrations x<0.3 and at x=0.3 it is possible to find anisotropies coming from clusters formed with specific concentrations of Gd^{3+} and Ce^{3+}, therefore, the piezoelectricity recently found for this material at this concentration has an anisotropic nature seen for first time in this material by RAS measurements. With a homemade code specific for this technique, it was possible to fit the RAS data in the presence of a magnetic field in polar configuration, The magnetic influence was observed from 2 eV to 4 eV where the *4f* transition and *F-Centers* emissions are found, so emissions in this range could have magnetic influence, however by micro-photoluminescence it was observed the crucial dependence of these emission centers as the thickness decreases.

At low Gd concentrations, the lattice parameter shows negligible variations and the material behaves as Gd doped CeO_2 (CeO_2:Gd) with an electron concentration that varies from 6.5×10^{14} to 9.4×10^{16} cm^{-3}. The Gd doping of CeO2 was confirmed by current – voltage measurements of two heterojunctions using CeO_2:Gd as the active n-type layer. The diode and photovoltaic parameters were obtained showing the feasibility to use this material as an active layer in pn junctions and Si based electronics

Appendix I

```
%RAS-MAGO

clear all


Mat=dlmread('CeO2_90_BSp.txt');
Subst=dlmread('Subs_CoE.txt');

En=Mat(:,1)';

lamb=(1240./En).*10;

nm=Mat(:,2)';
km=Mat(:,3)';

ns=Subst(:,2)';
ks=Subst(:,3)';

%plot(En,ns)
%hold on
%plot(En,ks)
%hold on

%plot(En,nm)
%hold on
%plot(En,km)

Ang=5;


phi=0:5:10;
gam=0;

%Nm=2.87+ 1i*3.36;
%lamb=6328e-10;
Qc=0.336*10^4+ 1i*0.048*10^4;

d=250e-10;


%N2=0.12+ 1i*3.29;
```

```
SS=zeros(1,length(nm));

PP=zeros(1,length(nm));
Nm=zeros(1,length(nm));
N2=zeros(1,length(nm));
Ang2=zeros(1,length(nm));
rss=zeros(1,length(nm));
rsp=zeros(1,length(nm));
rps=zeros(1,length(nm));
rpp=zeros(1,length(nm));


for a=1:length(phi)

for i=1: length(nm)
Nm(i)=nm(i) + 1i*km(i);
N2(i)=ns(i) + 1i*ks(i);

Ang2(i)=asind( sind(Ang)/(real(Nm(i)))  );
%Ang2=sqrt(1 - ( ( (sind(Ang(i)))^2)/((Nm)^2)  )   );



A1=[1 0 1 0; 0 cosd(Ang) 0 -cosd(Ang); 0 -1 0 -1; cosd(Ang) 0 -
cosd(Ang) 0];

InA1=inv(A1);


aly=sind(Ang2(i));
alz=cosd(Ang2(i));


gi=alz*cosd(phi(a)) + aly*sind(phi(a))*sind(gam);
gr=-alz*cosd(phi(a)) + aly*sind(phi(a))*sind(gam);

%Matrix elements A(2,:)
Ab1=(1i/2)*(aly/alz)*Qc*( (aly*gi) - (2*sind(phi(a))*cosd(gam)) );
Ab2= alz + (1i*aly*sind(phi(a))*cosd(gam)*Qc );
Ab3= (-1i/2)*(aly/alz)*Qc*( (aly*gr) - (2*sind(phi(a))*cosd(gam)) );
Ab4= -alz + (1i*aly*sind(phi(a))*cosd(gam)*Qc);

Ac1=(1i/2)*Nm(i)*gi*Qc;
Ac2=-Nm(i);
Ac3=(1i/2)*Nm(i)*gr*Qc;
Ac4=-Nm(i);

Ad1=Nm(i)*alz;
Ad2=((Nm(i)*1i)/(2*alz))*gi*Qc;
Ad3=-Nm(i)*alz;
Ad4=-((Nm(i)*1i)/(2*alz))*gr*Qc;
```

```
Am= [1 0 1 0;Ab1 Ab2 Ab3 Ab4; Ac1 Ac2 Ac3 Ac4; Ad1 Ad2 Ad3 Ad4 ];

IAm=inv(Am);
%final matrix A------------


Af=[1 0 1 0; 0 cosd(Ang2(i)) 0 -cosd(Ang2(i)); 0 -N2(i) 0 -N2(i);
N2(i)*cosd(Ang2(i)) 0 -N2(i)*cosd(Ang2(i)) 0];









%-------------------------------------------------------------
U=exp(-1i*((2*pi)/lamb(i))*Nm(i)*d*alz);
Si=(pi/lamb(i))*Nm(i)*d*(Qc/alz)*gi;
Sr=(pi/lamb(i))*Nm(i)*d*(Qc/alz)*gr;


D=[U (U*Si) 0 0; (-U*Si) U 0 0; 0 0 (1/U) (-(1/U)*Sr);0 0 ((1/U)*Sr)
(1/U)];


LL=Am*D*IAm;

W=InA1*LL*Af;

G=[W([1 5]);W([2 6])];

InvG=inv(G);

I=[W([3 7]);W([4 8])];

r=I*InvG;


rss(i)=r(1,1);
rps(i)=r(2,1);

rsp(i)=r(1,2);
rpp(i)=r(2,2);
```

```
SS(i)=(r(2,1)/r(1,1));

PP(i)=(r(1,2)/r(2,2));




end

RSS1=real(SS);
RSS2=real(PP);

ISS1=imag(SS);

RD=RSS1-RSS2;


RPP1=(-1)*real(PP);
IPPI=imag(PP);
%------------ s ---------------
%plot(En,imag(rsp)); %s Kerr rotation
%hold on


plot(En,RD); %s ellipticity
hold on
%figure

%-------- P -------------------
%plot(Ang,RPP1) %p Kerr rotation
%hold on

%xlabel()


%plot(Ang,IPPI) %p Ellipticity
%hold on

end
file01=table(En',RD');
writetable(file01,'RAS-MAGOP.txt');
```

Finally, to end this thesis I would like to recommend you a book “La conjetura de Euler” whose end I didn’t understand until these days and I leave you the following statement to conclude.

Entre todo el caos y con la precisión que está hecho nuestro universo, comprendí que yo no tenía tanta fortaleza como pensaba, por lo tanto Dios existe.

Acknowledgments:

To God for allowing me to finish my studies and face this part of my life. I want to thank my parents for their unconditional support, and I am glad to have both of you in this part of my life, giving me an example of how to face adverse situations.

I would like my brothers and sisters to know that despite our differences we always remain together, I appreciate each one of you and I would like to use this moment to thank you for supporting me in the misfortunes that have befallen me

I would like to express my gratitude to my advisor Dr. Ángel Gabriel Rodríguez Vázquez, thank you for your unconditional support. To Dr. Raúl for trusting me and helping me with my stay and to the evaluation committee, Dr. Harumi and Dr. Hugo (Dr. Hugo, thank you for teaching me during my bachelor's degree and what good talks about reading we have had).

To my great family, "Los Arteaga" for their great support and understanding during every Sunday meal, especially to Polar for helping me in a crucial and funny stage of my life (Nemo, thank you for taking me to that cruise to " drink a juice", I sincerely enjoyed it a lot).

To the López Arteaga family, because with them I can share my love for reading and have very comfortable, comforting and learning conversations, here I want to highlight the admiration I have for Arlo and Lalo, the first in music and the second in science.

It is also time to thank Veronica, who was with me throughout these four years with a lot of patience and understanding, always supporting me in everything.

A special thanks to Joa and Aida for their unconditional help.

To my little family during my stay in Linz: Saúl, Claudia, Luis, Karí and the good Qiu Qiu, I take this opportunity to tell Karí that she is a very good friend and that her support in this process was unconditional. To Quique I would like to thank him for being like a brother during all this time, what good parties, beers we drank and that December with Glühwein playing cuphead made me feel at home.

Special thanks to the Coordination for the Innovation and Application of Science and Technology (CIACYT), for allowing me to use the laboratory facilities and equipment, as well as to CONACYT for the support with the doctoral scholarship.

I would like to thank my friends from CIACYT: Carlos, Sara, Checo, Perea and Fredy whom I have had incredible moments with.

I have left for the end a very important person in my life, Pablo Lopez, who showed me one of my greatest passions, the music that eventually became in "Xtabay" and one of the things I will never leave, composition and music.

Agradecimientos:

A Dios por permitirme concluir mis estudios, y afrontar este momento de mi vida. Quiero agradecer el apoyo incondicional de mis padres y doy gracias por tenerlos a ambos en esta etapa de mi vida, dándome ejemplo de cómo afrontar las situaciones adversas.

Quiero que sepan mis hermanos, que a pesar de nuestras diferencias siempre permanecemos unidos, que aprecio a cada uno de ustedes y aprovecho este momento para darles las gracias por apoyarme en las desventuras que me han tocado.

Externo aquí mi agradecimiento a mis Asesor el Dr. Ángel Gabriel Rodríguez Vázquez, gracias por su apoyo incondicional. Al Dr, Raúl por confiar en mi y ayudarme con lo de mi estancia y también al comité evaluador, la Dra. Harumi y el Dr. Hugo (Dr. Hugo, gracias por haberme formado en la licenciatura y que buenas pláticas sobre lectura hemos tenido)

A mi gran familia, “Los Arteaga” por su enorme apoyo y comprensión durante cada comida dominical, especialmente al Polar por haberme ayudado en una etapa crucial y divertida de mi vida (Nemo gracias por haberme llevado a ese crucero a “tomarme un juguito”, lo disfruté mucho sinceramente)

A la familia López Arteaga, porque con ellos puedo compartir mi gusto por la lectura y tener platicas demasiado cómodas, confortantes y de mucho aprendizaje, aquí quiero resaltar la admiración que tengo por Arlo y Lalo el primero en lo musical y el segundo en lo científico.

También es momento de agradecer a Verónica, quien me acompañó a lo largo de estos cuatro años con mucha comprensión y apoyándome siempre en todo.

Un especial agradecimiento a Joa y Aida por su apoyo incondicional.

A mi pequeña familia durante mi estancia en Linz: Saul, Claudia, Luis, Karí y el buen Qiu Qiu, aprovecho para decirle a Karí que es muy buena amiga y que fue incondicional su apoyo en este proceso. A quique quisiera darle las gracias por haberse portado como un hermano durante todo este tiempo, que buenas fiestas, buenas cervezas las que nos tomamos y ese diciembre con Glühwein jugando cuphead hizo sentirme como en casa.

Doy un espacio para agradecer a mis amigos de Ciacyt: Carlos, Sara, Checo, Perea y Fredy con quienes he pasado momentos increíbles.

Un especial agradecimiento a la Coordinación para la Innovación y Aplicación de la Ciencia y la Tecnología (CIACYT), por permitirme el uso de las instalaciones y equipo de laboratorio, como también a CONACYT por el apoyo con la beca de doctorado.

He dejado para el final a una persona muy importante en mi vida a Pablo López quién me mostro una de mis grandes pasiones, la música que se convirtió con el tiempo en “Xtabay” y en una de las cosas que jamás dejaré, la composición y la música.

References.

[1] X. Wang *et al.*, “Enhancement of Sb2Se3 thin-film solar cell photoelectric properties by addition of interlayer CeO2,” *Sol. Energy*, vol. 188, no. April, pp. 218–223, 2019, doi: 10.1016/j.solener.2019.05.028.

[2] X. Wang *et al.*, “Cerium oxide standing out as an electron transport layer for efficient and stable perovskite solar cells processed at low temperature,” *J. Mater. Chem. A*, vol. 5, no. 4, pp. 1706–1712, 2017, doi: 10.1039/c6ta07541j.

[3] L. E. Ríos-Saldaña, V. D. Compeán-García, H. Moreno-García, and A. G. Rodríguez, “Improvement of the conversion efficiency of as-deposited Bi2S3/PbS solar cells using a CeO2 buffer layer,” *Thin Solid Films*, vol. 670, no. March 2018, pp. 93–98, 2019, doi: 10.1016/j.tsf.2018.12.017.

[4] Y. D. Kim *et al.*, “Degradation studies of ceria-based solid oxide fuel cells at intermediate temperature under various load conditions,” *J. Power Sources*, vol. 452, no. December 2019, p. 227758, 2020, doi: 10.1016/j.jpowsour.2020.227758.

[5] W. Y. Hernández, O. H. Laguna, M. A. Centeno, and J. A. Odriozola, “Structural and catalytic properties of lanthanide (La, Eu, Gd) doped ceria,” *J. Solid State Chem.*, vol. 184, no. 11, pp. 3014–3020, 2011, doi: 10.1016/j.jssc.2011.09.018.

[6] J. A. Kilner and C. D. Waters, “The effects of dopant cation-oxygen vacancy complexes on the anion transport properties of non-stoichiometric fluorite oxides,” *Solid State Ionics*, vol. 6, no. 3, pp. 253–259, 1982, doi: 10.1016/0167-2738(82)90046-7.

[7] H. Duncan and A. Lasia, “Influence of the electrode nature on conductivity measurements of gadolinia-doped ceria,” *Solid State Ionics*, vol. 176, no. 15–16, pp. 1429–1437, 2005, doi: 10.1016/j.ssi.2005.03.018.

[8] G. Accardo, C. Ferone, R. Cioffi, D. Frattini, L. Spiridigliozzi, and G. Dell’Agli, “Electrical and microstructural characterization of ceramic gadolinium-doped ceria electrolytes for ITSOFCs by sol-gel route,” *J. Appl. Biomater. Funct. Mater.*, vol. 14, no. 1, pp. e35–e41, 2016, doi: 10.5301/jabfm.5000265.

[9] W. H. Weber, K. C. Hass, and J. R. McBride, “Raman study of CeOz. Second-order scattering, lattice dynamics, and particle-size effects,” *Phys. Rev. B*, vol. 48, no. 1, pp. 178–185, 1993, doi: 10.1103/PhysRevB.48.178.

[10] J. R. McBride, K. C. Hass, B. D. Poindexter, and W. H. Weber, “Raman and x-ray studies of Ce1-xRExO2-y, where RE=La, Pr, Nd, Eu, Gd, and Tb,” *J. Appl. Phys.*, vol. 76, no. 4, pp. 2435–2441, 1994, doi: 10.1063/1.357593.

[11] J. Roh, S. H. Hwang, and J. Jang, “Dual-Functional CeO 2 :Eu 3+ Nanocrystals for Performance-Enhanced Dye-Sensitized Solar Cells,” 2014.

[12] P. Patsalas, S. Logothetidis, and C. Metaxa, “Optical performance of nanocrystalline transparent ceria films,” *Appl. Phys. Lett.*, vol. 81, no. 3, pp. 466–468, 2002, doi: 10.1063/1.1494458.

[13] V. Seminko *et al.*, “Defect and intrinsic luminescence of CeO2 nanocrystals,” *Phys. Status Solidi Basic Res.*, vol. 254, no. 4, 2017, doi: 10.1002/pssb.201600488.

[14] S. Kurtaran, M. Kellegöz, and S. Köse, “Characterization of Gd doped CeO2 thin films grown by ultrasonic spray pyrolysis,” *Opt. Mater. (Amst).*, vol. 117, no. April, 2021, doi: 10.1016/j.optmat.2021.111144.

[15] M. Veis *et al.*, “Optical and magneto-optical properties of Co-doped CeO2-δ films in the 0.5 to 4eV range,” *J. Appl. Phys.*, vol. 115, no. 17, pp. 2–6, 2014, doi: 10.1063/1.4867961.

[16] A. Bandyopadhyay, B. J. Sarkar, S. Sutradhar, J. Mandal, and P. K. Chakrabarti, “Synthesis, structural characterization, and studies of magnetic and dielectric properties of Gd3+ doped cerium oxide (Ce0.90Gd0.10O2−δ),” *J. Alloys Compd.*, vol. 865, p. 158838, 2021, doi: 10.1016/j.jallcom.2021.158838.

[17] T. Gürel and R. Eryiğit, “Ab initio pressure-dependent vibrational and dielectric properties of CeO2,” *Phys. Rev. B - Condens. Matter Mater. Phys.*, vol. 74, no. 1, pp. 1–5, 2006, doi: 10.1103/PhysRevB.74.014302.

[18] T. P. Pearsall, *Strained-Layer Superlattices*, vol. 32, no. C. 1990.

[19] F. Cerdeira, C. J. Buchenauer, F. H. Pollak, and M. Cardona, “Stress-induced shifts of first-order Raman frequencies of diamond- and zinc-blende-type semiconductors,” *Phys. Rev. B*, vol. 5, no. 2, pp. 580–593, 1972, doi: 10.1103/PhysRevB.5.580.

[20] N. Y. (G. K. Horton and A. A. Maradudin, eds.). North Holland, “Dynamical properties of Solids.”

[21] S. Patil, S. Seal, Y. Guo, A. Schulte, and J. Norwood, “Role of trivalent la and Nd dopants in lattice distortion and oxygen vacancy generation in cerium oxide nanoparticles,” *Appl. Phys. Lett.*, vol. 88, no. 24, pp. 2004–2007, 2006, doi: 10.1063/1.2210795.

[22] *Formulas from Algebra Cauchy-Schwarz Inequality Formulas from Geometry Formulas from Trigonometry*. .

[23] J. Rashidinia and S. Sharifi, “Survey of B-spline functions to approximate the solution of mathematical problems,” *Math. Sci.*, vol. 6, no. 1, pp. 1–8, 2012, doi: 10.1186/2251-7456-6-48.

[24] L. F. Lastras-Martínez *et al.*, “Effects of substrate orientation on the optical anisotropy spectra of GaN/AIN/Si heterostructures in the energy range from 2.0 to 3 5ev,” *J. Appl. Phys.*, vol. 111, no. 2, pp. 0–5, 2012, doi: 10.1063/1.3677949.

[25] M. C. Onbasli *et al.*, “Optical and magneto-optical behavior of Cerium Yttrium Iron Garnet thin films at wavelengths of 200-1770 nm,” *Sci. Rep.*, vol. 6, no. March, 2016, doi: 10.1038/srep23640.

[26] G. van der Laan, E. Arenholz, E. Navas, A. Bauer, and G. Kaindl, “Magnetic circular dichroism and orbital momentum coupling in photoemission from Gd(0001),” *Phys. Rev. B - Condens. Matter Mater. Phys.*, vol. 53, no. 10, pp. R5998–R6001, 1996, doi: 10.1103/PhysRevB.53.R5998.

[27] N. V. Skorodumova, R. Ahuja, S. I. Simak, I. A. Abrikosov, B. Johansson, and B. I. Lundqvist, “Electronic, bonding, and optical properties of CeO2 and Ce2O3 from first principles,” *Phys. Rev. B - Condens. Matter Mater. Phys.*, vol. 64, no. 11, pp. 1151081–1151089, 2001, doi: 10.1103/physrevb.64.115108.

[28] M. Effects, “Fundamental magneto-optics,” vol. 4203, no. April 1990, 2000.

[29] J. Zak, E. R. Moog, C. Liu, and S. D. Bader, “Universal approach to magneto-optics,” *J. Magn. Magn. Mater.*, vol. 89, no. 1–2, pp. 107–123, 1990, doi: 10.1016/0304-8853(90)90713-Z.

[30] F. Haidu, M. Fronk, O. D. Gordan, C. Scarlat, G. Salvan, and D. R. T. Zahn, “Dielectric function and magneto-optical Voigt constant of Cu2O: A combined spectroscopic ellipsometry and polar magneto-optical Kerr spectroscopy study,” *Phys. Rev. B - Condens. Matter Mater. Phys.*, vol. 84, no. 19, 2011, doi: 10.1103/PhysRevB.84.195203.

[31] G. S. Krinchik and a. V. Artem’ev, “MAGNETO-OPTICAL PROPERTIES OF Ni, Co, AND Fe IN THE ULTRAVIOLET VISIBLE, AND INFRARED PARTS OF THE SPECTRUM,” *Sov. Phys. JETP*, vol. 26, no. 6, pp. 1080–1085, 1968.

[32] J. A. Purton, A. Archer, N. L. Allan, and D. S. D. Gunn, “Growth of nano-domains in Gd-CeO2 mixtures: Hybrid Monte Carlo simulations,” *J. Mater. Chem. A*, vol. 4, no. 12, pp. 4592–4602, 2016, doi: 10.1039/c5ta07506h.

[33] T. Sato and S. Tateyama, “Temperature Dependence of the Linewidth of First-

Order Raman Spectrum for CdF2 Crystals," *Phys. Status Solidi*, vol. 113, no. 1, pp. 291–299, 1982, doi: 10.1002/pssb.2221130130.

[34] A. Nakajima, A. Yoshihara, and M. Ishigame, "Defect-induced Raman spectra in doped CeO2," *Phys. Rev. B*, vol. 50, no. 18, pp. 13297–13307, 1994, doi: 10.1103/PhysRevB.50.13297.

[35] M. P. van Dijk, A. J. Burggraaf, A. N. Cormack, and C. R. A. Catlow, "Defect structures and migration mechanisms in oxide pyrochlores," *Solid State Ionics*, vol. 17, no. 2, pp. 159–167, 1985, doi: 10.1016/0167-2738(85)90067-0.

[36] P. Burroughs, A. Hamnett, A. F. Orchard, and G. Thornton, "Satellite Structure in theX-Ray Photoelectron Spectra of some Binary and Mixed Oxides of Lanthanum and Cerium," *J. Chem. Soc., Dalt. Trans.*, no. 1686, pp. 1686–1698, 1976.

[37] P. Patsalas, S. Logothetidis, and C. Metaxa, "Optical performance of nanocrystalline transparent ceria films," *Appl. Phys. Lett.*, vol. 81, no. 3, pp. 466–468, 2002, doi: 10.1063/1.1494458.

[38] H. Borchert *et al.*, "Electronic and chemical properties of nanostructured cerium dioxide doped with praseodymium," *J. Phys. Chem. B*, vol. 109, no. 12, pp. 5728–5738, 2005, doi: 10.1021/jp045828c.

[39] H. Borchert *et al.*, "Nanostructured, Gd-doped ceria promoted by Pt or Pd: Investigation of the electronic and surface structures and relations to chemical properties," *J. Phys. Chem. B*, vol. 109, no. 43, pp. 20077–20086, 2005, doi: 10.1021/jp051525m.